

Mid-IR observations of circumstellar disks[★]

Part III. A mixed sample of PMS stars and Vega-type objects

O. Schütz¹, G. Meeus², M. F. Sterzik¹, and E. Peeters^{3,4,5}

¹ European Southern Observatory, Alonso de Cordova 3107, Santiago 19, Chile
e-mail: oschuetz@eso.org

² Astrophysikalisches Institut Potsdam, An der Sternwarte 16, 14482 Potsdam, Germany

³ NASA Ames Research Center, MS 245-6, Moffett Field, CA 94035, USA

⁴ SETI Institute, 515 N. Whisman Road, Mountain View, CA 94043, USA

⁵ The University of Western Ontario, London, ON N6A 3K7, Canada

Received 18 August 2006 / Accepted 17 April 2009

ABSTRACT

We present new mid-infrared spectra of 15 targets (1 FU Orionis object, 4 Herbig Ae stars, 5 T Tauri stars, and 5 Vega-type stars), obtained with the TIMMI2 camera at La Silla Observatory (ESO). Three targets are members of the β Pic moving group (HD 155 555, HD 181 296, and HD 319 139). PAH bands are observed towards the T Tauri star HD 34 700 and the Herbig Ae star PDS 144 N. For HD 34 700, the band profiles indicate processed PAHs. The spectrum of the Vega-type object η Corvi (HD 109 085), for which a resolved disk at sub-mm wavelengths is known, appears stellar between 8–13 μm , but a small excess emission was reported by Spitzer observations. Similarly, no indication of circumstellar matter at mid-infrared wavelengths is found towards the Vega-like stars HD 3003, HD 80 951, HD 181 296, and, surprisingly, the T Tauri system HD 155 555. The silicate emission features of the remaining eight sources are modelled with a mixture of silicates of different grain sizes and composition. Unprocessed dust dominates FU Ori, HD 143 006, and CD-43 344. Large amorphous grains are the main dust component around HD 190 073, HD 319 139, KK Oph, and PDS 144 S. Both small grains and crystalline dust is found for the Vega-type HD 123 356, with a dominance of small amorphous grains. We show that the infrared emission of the binary HD 123 356 is dominated by its late-type secondary, but optical spectroscopy is still required to confirm the age of the system and the spectral class of the companion. For most targets, this is their first mid-infrared spectroscopic observation. We investigate trends between stellar, disk, and silicate properties and confirm correlations identified in previous studies. Several objects present an exciting potential for follow-up high-resolution disk studies.

Key words. methods: observational – techniques: spectroscopic – stars: circumstellar matter – infrared: stars – stars: planetary systems: protoplanetary disks – stars: pre-main sequence

1. Introduction

Until now a full understanding of dust evolution in pre-main sequence (PMS) disks and the survival of debris disks is lacking. In terms of their dust evolution, we need to distinguish between the two disk types. For an in-depth discussion of gas and dust evolution in circumstellar disks, we refer the reader to the review by Meyer et al. (2007).

Primordial PMS disks largely reflect the grain size distribution of the interstellar medium (ISM), while more evolved PMS disks experience grain growth and crystallisation. However, there is no global correlation between dust properties and age, not even for individual spectral types. Schegerer et al. (2006) re-analysed the mid-infrared silicate emission features of 27 T Tauri stars (TTS) and found that the overall degree of crystallinity in T Tauri disks correlates neither with stellar age nor luminosity. By resolved interferometric observations, van Boekel et al. (2004) showed that a higher amount of crystalline dust is seen in close proximity to the star than in the outer disk regions. In

an analysis of 40 TTS and 7 HAeBe stars, Kessler-Silacci et al. (2006) found a correlation with spectral type for the ratio of strength-to-shape in the N -band silicate feature, but no relationship with stellar age or disk evolutionary status. Therefore, the observed grain sizes in PMS disks must also depend on other factors such as, e.g., close companions, or turbulence and gas content in the disk, while the exact dependencies thereof remain unknown. Kessler-Silacci et al. (2007) demonstrated that the disk region probed by the 10 μm silicate emission features, is related to stellar luminosity, which could explain the correlation of grain size with spectral type.

Debris disks – also referred to as Vega-type objects – are often characterised by their lack of gas, so that the dust dynamics is no longer influenced by that of the gas. The presence of small dust particles in these disks points towards a continuous replenishment of the dust grains, e.g., by collisions between planetesimals, asteroids, or comets. By means of collisional cascades significant amounts of small grains can be produced, down to grain sizes that are easily removed by radiation pressure on short timescales, and therefore, without replenishment would not be expected to be present in the disk. Song et al. (2005) found a surprisingly strong silicate feature for the ~ 300 Myr old star BD+20 307, which they explained by the release of secondary

[★] Based on observations made at the European Southern Observatory, obtained under program IDs 076.C-0634(A) and 077.C-0054(A), during TIMMI2 technical time as well as collected from the ESO/ST-ECF Science Archive Facility.

dust after the destruction of asteroids. The emission peak shortward of $10\ \mu\text{m}$ in its spectrum indicates rather small grains. In Schütz et al. (2005b, hereafter Paper II), we discussed a similar – but much younger – main-sequence object, HD 113 766, which shows large amounts of crystalline secondary dust, possibly released by collisions in a planetesimal belt. By applying spatially resolved spectroscopy to β Pic, Okamoto et al. (2004) were able to trace the origin of secondary dust towards the location of putative planetesimal belts. HD 69 830 is another system with secondary debris dust in the form of warm, small, crystalline silicates (Beichman et al. 2005), possibly resulting from the disruption of an asteroid within 1 AU from the star (Lisse et al. 2007). Interestingly, this system is also known to host three Neptune-sized planets (Lovis et al. 2006).

The present paper continues our previous mid-infrared (MIR) spectroscopic studies of circumstellar disks. In Schütz et al. (2005a, hereafter Paper I), we described our strategy and dust emission models, and analysed a sample of pre-main sequence stars. Vega-type objects with debris disks were studied with the same methods in Schütz et al. (2005b, Paper II).

This contribution describes new mid-infrared spectra of circumstellar disks. We selected targets with infrared excess that have not yet been discussed in depth in the literature, i.e., objects which were suspected to be disk candidates, but for which no MIR spectroscopy had been obtained before. Several isolated targets were unobserved by Spitzer, since they were not included in the surveys of open clusters and moving groups. We re-observed targets where newer or higher SNR data were required, as for HD 34 700. A MIR spectrum of KK Oph had already been published, however, it was not analysed with the methods that we present here. We included the well studied object FU Ori to enable a comparison with other FU Orionis targets from Paper I. Table 1 summarises our targets and their stellar parameters. In Sect. 2, we describe the observations and data reduction. Section 3 discusses the spectral energy distributions (SEDs) and methods for analysing the emission feature in the 8–13 μm spectra. In Sect. 4, we describe observed trends in the dust properties. A summary of our results is given in Sect. 6. The known properties of each target are described in detail in the Appendix. It is our goal to contribute a piece to the puzzle of disk and dust evolution around young stars.

2. Observations and data reduction

TIMMI2. The principal data described in this work were obtained with the ESO TIMMI2 camera (Käufl et al. 2003) at La Silla Observatory. We performed most of the observations during run 077.C-0054(A) in June 2006, supported by further data retrieved from the ESO/ST-ECF Science Archive¹, which was originally observed in March 2003 (targets HD 109 085, HD 123 356 and HD 143 006; ESO program 070.C-0743(A); PI J.-C. Augereau) and July 2003 (target KK Oph; ESO program 071.C-0438(A); PI H. Linz). Further data were collected during TIMMI2 technical nights in October 2005 and January 2006. Table 2 summarises the origin of all data.

Imaging data were obtained with a $0.20''/\text{pixel}$ scale, corresponding to a $64'' \times 48''$ field of view. For most targets, the nodding direction was perpendicular to the chop throw, resulting in four images of the source in the coadded frame, each carrying 25% of the flux. Some archive data, however, had the nod parallel to the chop, giving three images of the source, with the central one carrying 50% of the flux. We applied aperture photometry

with radii r_{ap} between 2.6 pixel and 4.7 pixel, depending on the target. The optimal radii were derived from curves of growth and averaged over the radii obtained for each of the beams, to account for detector inhomogeneities. We estimate the error in the photometry by calculating the mean of the measurement errors for each beam. The background level was determined by measuring the mean sky value per pixel around each beam in an annulus centred on the star with inner radius $r_{\text{ap}} + 10$ pixel and outer radius $r_{\text{ap}} + 20$ pixel (resulting in a maximum outer radius of $5''$, while the chopping amplitude is $10''$). Photometric standard stars were selected from a list of MIR standards by Cohen (1998) and observed approximately each 2 h.

N-band spectra were obtained between 8–13 μm by applying a standard chopping and nodding technique along the $1.2''$ slit (for archive data and technical time) or the $3''$ slit (run 077.C-0054(A)) with a throw of $10''$. The spectral resolution of the used $10\ \mu\text{m}$ low-resolution grism is $0.02\ \mu\text{m}/\text{pixel}$ ($\lambda/\delta\lambda \sim 160$). Airmass and on-source integration times of the observations are listed in Table 2. Standard stars for telluric correction and flux calibration were selected from the list of Cohen (1998) and observed close in time and airmass.

The spectroscopic frames were debiased and checked for correct slit alignment along the detector, i.e., whether the spectrum is aligned with the x-axis. After coadding the positive and negative nodding positions, the extraction profile was determined from the cross dispersion profile: the target spectrum was extracted along a profile width where the SNR exceeds 2.5 times the noise of the background. We furthermore applied an airmass correction described in Schütz & Sterzik (2005) and correlated the spectrophotometric calibration with the obtained *N*-band photometry. The wavelength calibration was optimised using the atmospheric absorption features of ozone ($9.58\ \mu\text{m}$) and CO_2 ($11.73\ \mu\text{m}$, $12.55\ \mu\text{m}$) in addition to the given TIMMI2 wavelength calibration table, i.e., shifts were applied to minimise the residual division between the atmospheric features in standard stars and target spectra. When atmospheric conditions were unstable between observations of target and standard star, leaving uncorrectable ozone features around $9.5\ \mu\text{m}$, we removed these remnant features from the spectra. By comparing data from different nights and applying several standard stars for comparison, the exact position of the ozone remnant feature can be identified. Depending on the atmospheric quality, this leaves gaps of different sizes up to a maximum range of between 9.4 and $9.9\ \mu\text{m}$. The SNR in our target spectra, averaged between 8–12 μm , ranges between 10 and about 70 for all objects, with a minimum SNR in the spectra of HD 3003 and HD 319 139, while the highest SNR is obtained for FU Ori and KK Oph.

Spitzer. HD 34 700 is also observed with the IRS onboard the Spitzer Space Telescope (Werner et al. 2004) (AOR key = 3 584 768, GTO program of J. Houck). The spectra were taken with the Short-Low (SL, 5–15 μm) and Short-High (SH, 10–20 μm) modules (Houck et al. 2004) with a resolving power of $R = 60$ –128 and 600, respectively. The basic data reduction was performed by the standard IRS pipeline S13 at the Spitzer Science Center (SSC). Subsequently, bad pixels were removed with IRSCLEAN (available from the SSC website²) and a standard point-source extraction was performed using SMART (Higdon et al. 2004): tapered column extraction for SL data (i.e., the width of the extraction scales with wavelength and equals $7.2''$ at $6\ \mu\text{m}$); full aperture extraction for SH data ($4.7'' \times 11.3''$).

¹ <http://archive.eso.org>

² <http://ssc.spitzer.caltech.edu>

Further auxiliary data. During the discussion of two targets – HD 109085 and HD 123356 – we refer to individual data obtained either with VISIR (Lagage et al. 2004) or SOFI (Moorwood et al. 1998).

3. Analysis

3.1. Spectral energy distributions

Together with fluxes from the literature in the passbands UBVR, JHK (2MASS), 12, 25, 60 and 100 μm (IRAS), we used the TIMMI2 photometry in Table 2 to construct a spectral energy distribution (SED) for our targets. In Figs. 1–3, the resulting optical to mm spectral energy distributions are displayed. To emphasise the non-stellar contribution to the SED, we plotted a Kurucz atmosphere model (Kurucz 1994) with the stellar parameters from Table 1, normalised to the V -band flux. For FU Ori, we did not plot a Kurucz model, since for this kind of object the V -band flux most likely originates in the star and the hot inner part of the outbursting disk (cf. Sect. A.1). Where required, we reddened the Kurucz model with the extinction A_v given in Table 1. The photometry to construct the SEDs was taken from Hutchinson et al. (1990), Henning et al. (1994), Sylvester et al. (1996), Coulson et al. (1998), Malfait et al. (1998), Mannings & Barlow (1998), Sylvester & Mannings (2000), Sylvester et al. (2001), Jayawardhana et al. (2001), Mamajek et al. (2004), Natta et al. (2004), Sheret et al. (2004), Wyatt et al. (2005), Perrin et al. (2006), and the catalogs JP11, 2MASS, IRAS, and SIMBAD.

The SED of HD 155555 can be explained entirely by stellar emission, while for HD 3003, HD 80951, HD 109085, and HD 181296, the IR excess begins longward of 25 μm . We, therefore, do not consider those objects in our dust analysis. For the other targets, a near-infrared (NIR) excess is seen, starting longward of the L -band for HD 34700 as well as HD 319139, and around 1 μm for the remaining eight targets.

For HD 109085 (alias η Crv), we obtained $Q1$ band (17.7 μm) imaging with VISIR during run 076.C-0634(A) in March 2006. Using a standard chopping technique η Crv was observed with a throw of 10'' at an airmass of 1.03, while the standard star (HD 99167) was obtained at airmass 1.35. Standard data reduction and photometric extraction was applied, including a correction for the atmospheric extinction. The derived photometric flux was 1.59 Jy (± 0.10 Jy). Subtraction of the PSF showed that the source was not resolved at 17.7 μm : the FWHM was 6.7 pixel (0.50'') for the standard star, while only 6.8 pixel (0.51'') for η Crv.

We determined from which component of HD 123356 the excess emission arises. The 2MASS photometry gives the combined fluxes of both sources but interestingly, the corresponding 2MASS coordinates seem to be centered on the secondary. With SOFI images obtained during thick clouds in May 2006, we were able to separate the emission components and found that the secondary dominates the IR. The relative NIR brightness difference between secondary and primary amounts to 3.3 mag in filter NB1.19, 4.0 mag in NB1.71 and FeII-H, and 4.2 mag in NB2.09. With this information, it was possible to divide the 2MASS fluxes between both components and to plot a resolved SED (see Fig. 3). From the $VJHK$ colors of both stars, the primary appears to be a F7-G1 star, in agreement with the SIMBAD classification, while the secondary seems to be either a very late M-type or it suffers extinction. In TIMMI2 MIR data, we only could detect one isolated source. Although astrometry is not possible using TIMMI2 data, with the observations discussed above,

we can safely assume that we only see the secondary in the MIR. In the SED, we plot Kurucz models for both components.

3.2. Dust properties

In Figs. 4–6 and 8, we show the N -band spectra for our targets. To quantify the differences between the sources and determine the composition of the circumstellar dust, we adopted the same procedure as described in Sect. 4 of Paper I, which is summarised below in Sect. 3.2.1. For further details, we refer to Paper I. Since two objects exhibit strong PAH emission, a description of PAH classes is given in Sect. 3.2.4.

3.2.1. Silicates

When stars form out of their parental cloud, the material in their disks is assumed to have a similar *initial* composition as in the interstellar medium, in which amorphous silicates are the main component observed at 10 μm (e.g., Kemper et al. 2004). Changes in the composition, structure, and size are expected to occur during the subsequent evolution of the star+disk system, possibly leading to a planetary system. Laboratory experiments have suggested that, because of thermal annealing, amorphous silicates gradually turn into crystalline forsterite and silica (e.g., Rietmeijer 1989; Hallenbeck & Nuth 1997). Bouwman et al. (2001) found a correlation between the amount of forsterite and silica in the disks of Herbig Ae/Be (HAeBe) stars, indicating that thermal annealing indeed takes place in these objects. A similar correlation was also found for the lower-mass T Tauri stars (e.g. Meeus et al. 2003). These authors also concluded that the dust around HAeBe stars and T Tauri stars has very similar characteristics. In Paper II, we successfully modelled a sample of Vega-type stars with the same dust species as those found in young stellar objects. The above-mentioned dust species emit in the N band, making this an excellent window to study dust evolution in the inner parts of the circumstellar disk.

Our analysis is based on a method that is commonly used when analysing the dust features around 10 μm : fitting a continuum to the spectral range outside the feature, and then decomposing the continuum-subtracted emission feature by fitting a linear combination of absorption coefficients of different dust species, for a few selected sizes. For a deeper discussion of this method, we refer to Bouwman et al. (2001) and van Boekel et al. (2005). To derive the composition of the circumstellar dust, we model the spectra in Figs. 4–5 with a linear combination of emission features from the following dust species, which have been identified in the disks of pre-main sequence stars:

- Amorphous olivine ($[\text{Mg,Fe}]_2\text{SiO}_4$) with grain sizes of 0.1 and 2.0 μm , which we refer to as “small” and “large” grains. We used absorption coefficients of spherical grains based on laboratory experiments by Dorschner et al. (1995).
- Amorphous pyroxene ($[\text{Mg,Fe}]\text{SiO}_3$) with grain sizes of 0.1 and 2.0 μm . These absorption coefficients are also based on Dorschner et al. (1995).
- Crystalline silicates: magnesium forsterite (Mg_2SiO_4) and enstatite (MgSiO_3). The latter silicate, however, is rare even in young sources (cf. Paper I). Coefficients for forsterite are from Servoin & Piriou (1973), and for enstatite from Jaeger et al. (1998). Each of these silicates was modelled with both “small” and “large” grains.
- Silica (SiO_2) coefficients were taken from Spitzer & Kleinman (1961).

Table 1. Stellar parameters and known fluxes of our target sample.

Object	Class	Spectral type	T_{adopted} [K]	$(\log g)_{\text{adopted}}$	V [mag]	$F_{12\ \mu\text{m}}$ [Jy]	Age [Myr]	Ref.	d [pc]	Ref.	A_v [mag]	Ref.	Sep. ["]	Ref.
HD 3003	Vega	A0V	11 000	4.5	5.07	0.48	$50^{+197}_{-\dots}$	(1)	47	(9)	0.1 (?)	(26)
HD 34 700 A	TTS	G0IVe	6000	4.5	9.15	0.60	(10)	0.68	(19)	SB/5.2/9.2	(27)
HD 80 951 A	Vega	A1V	9500	4.5	6.00	0.44	220	(9)	0.3/7.1/48.2	(26)
HD 109 085	Vega	F2V	7000	4.5	4.31	2.18	1000^{+300}_{-300}	(2)	18	(11)	0.12	(20)
HD 123 356 AB	Vega	G1V/M?	6000 / 4000	4.5	10.0 / 12.2	1.36	(12)	0.16	(20)	2.5	(28)
HD 143 006	TTS	G5Ve	5750	4.5	10.21	0.86	~ 1	(3)	82	(13)	0.62	(21)
HD 155 555 ABC	TTS	G5IV/K0IV-V/M4.5	5750 / ...	4.5	6.88 / 13.0	0.69	12^{+8}_{-4}	(4)	32	(9)	SB/33.0	(26)
HD 181 296 A	Vega	A0Vn	9500	4.5	5.03	0.54	12^{+8}_{-4}	(4)	48	(9)	0.12	(20)	4.1	(29)
HD 190 073	HAeBe	A2IIIpe	9500	4.5	7.82	7.16	$1.2^{+0.6}_{-0.6}$	(5)	>290	(14)	0.19	(19)
HD 319 139	TTS	K5Ve / K7Ve	4250	4.5	10.44	0.45	$5.5^{+1.5}_{-1.5}$	(6)	83	(15)	≤ 0.12	(22)	SB	(30)
CD-43 344	TTS (?)	M2	4500	4.5	9.42	3.73	(10)	0.0	(20)
FU Ori A	FUOR	G0II	...	4.5	8.94	5.95	< 0.3	(7)	450	(16)	2.2	(23)	0.5	(31)
KK Oph A	HAeBe	A6Ve	8750	4.5	9.4–12.9	9.87	$7^{+10}_{-0.5}$	(8)	160	(17)	1.6	(24)	1.6	(32)
PDS 144 N	HAeBe	A2IV	8750	4.5	14.2	~ 1000	(18)	3.0	(25)	~ 5.0	(33)
PDS 144 S	HAeBe	A5V	8750	4.5	13.1	~ 1000	(18)	1.1	(25)	~ 5.0	(33)

References: Spectral types are obtained either from SIMBAD or one of the cited papers, if a more accurate classification is available in the literature. T_{adopted} and $(\log g)_{\text{adopted}}$ list the temperature and surface gravity which we used for the Kurucz atmosphere models. V -band magnitudes and IRAS $12\ \mu\text{m}$ fluxes are taken from the SIMBAD database. KK Oph shows variability in the visual. PDS 144 is not resolved by IRAS; its V -band fluxes were given by Perrin et al. (2006). Stellar ages: (1) Song et al. (2001), (2) Wyatt et al. (2005) and references therein, (3) Dunkin et al. (1997) and references therein, (4) mean age of the β Pic moving group as given in Zuckerman & Song (2001), (5) Catala et al. (2007), (6) Quast et al. (2000), (7) e.g. D'Angelo et al. (2000), (8) Carmona et al. (2007). Errors in the age determinations are quite heterogeneous, depending on the cited work. Distances are taken from (9) Hipparcos parallax, (10) uncertain Hipparcos parallax, (11) Wyatt et al. (2005), (12) The Hipparcos parallax was recently removed from SIMBAD and is likely not firm, (13) Sylvestre et al. (1996), (14) van den Ancker et al. (1998), (15) Quast et al. (2000), (16) e.g. Wang et al. (2004), (17) Hillenbrand et al. (1992), (18) Perrin et al. (2006) and references therein. Extinctions: (19) van den Ancker et al. (1998), (20) Sylvestre & Mannings (2000), (21) Malfait et al. (1998), (22) Hutchinson et al. (1990), (23) Kenyon et al. (1988), (24) Carmona et al. (2007), (25) Perrin et al. (2006). Stellar separations in multiple systems: (26) Dommanget & Nys (2002), (27) Sterzik et al. (2005), (28) Worley & Douglass (1997), (29) Lowrance et al. (2000), (30) Quast et al. (2000), (31) Wang et al. (2004), (32) Leinert et al. (1997), (33) Perrin et al. (2006). "SB" denotes a spectroscopic binary. Note on the multiplicity of HD 155 555: Although the SB components are not spatially resolved, we label them as A and B, since this naming convention existed already in the literature.

Table 2. Results from TIMMI2 photometry and spectroscopy.

Object	Origin	Airmass (N-spec)	t_{int} (N-spec) [min]	F_{N1} [Jy]	$F_{\text{N10.4}}$ [Jy]	$F_{\text{N11.9}}$ [Jy]	Ref.	N-spec features
HD 3003	technical	1.2	24	0.58 ± 0.03	0.32 ± 0.03	0.20 ± 0.10	...	stellar
HD 34 700	technical	1.2–1.5	60	0.79 ± 0.29	...	PAH
HD 80 951	077.C-0054	1.7	53	0.44 ± 0.03	(1)	stellar
HD 109 085	archive	1.1	12	1.51 ± 0.24	(2)	stellar
HD 123 356	archive	1.0	18	...	1.51 ± 0.05	1.68 ± 0.06	...	silicate emission
HD 143 006	archive	1.1	24	0.86 ± 0.06	(1)	silicate emission
HD 155 555	077.C-0054	1.3	58	0.46 ± 0.03	...	stellar
HD 181 296	077.C-0054	1.2	64	0.59 ± 0.05	stellar
HD 190 073	technical	1.5	12	7.16 ± 0.43	(1)	silicate emission
HD 319 139	077.C-0054	1.0	160	0.36 ± 0.03	...	silicate emission
CD-43 344	technical	1.1	24	3.78 ± 0.05	3.82 ± 0.05	3.04 ± 0.05	...	silicate emission
FU Ori	technical	1.4	20	...	6.00 ± 0.03	5.61 ± 0.03	...	silicate emission
KK Oph	archive	1.2	12	10.09 ± 0.05	...	10.71 ± 0.08	...	silicate emission
PDS 144 N	077.C-0054	1.0	32	1.74 ± 0.09	(3)	PAH
PDS 144 S	077.C-0054	1.0	13	2.49 ± 0.13	(3)	silicate emission

Results from TIMMI2 photometry and spectroscopy are merged in this table. The airmass and TIMMI2 integration times refer to *N*-band spectroscopy. Mid-IR photometry was obtained in the specified TIMMI2 filters with central wavelengths $8.6 \mu\text{m}$ (N1), $10.3 \mu\text{m}$ (N10.4) and $11.6 \mu\text{m}$ (N11.9). Errors represent the accuracy of the aperture photometry. Where no own measurements were available, e.g. for some archive data, we adapted data from (1) IRAS, (2) Wyatt et al. (2005) or (3) Perrin et al. (2006).

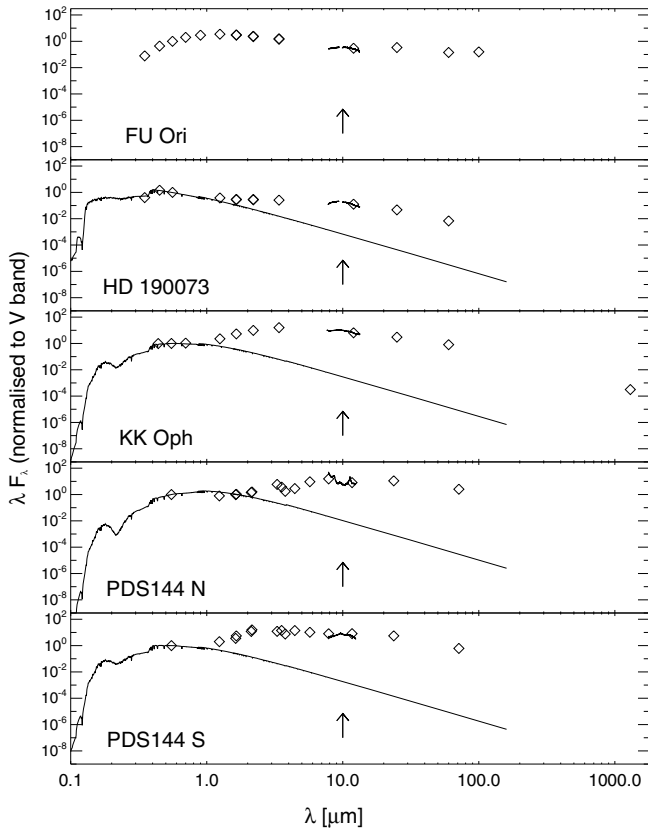


Fig. 1. Spectral energy distributions for FU Ori and the Herbig Ae stars. A Kurucz model is overplotted for all targets to represent the stellar contribution to the SED, apart from FU Ori as justified in the text. The profile of the *N*-band spectrum is indicated in the SEDs (at the position of the arrow) to show their agreement with the photometry. For PDS 144 N and S all IR fluxes are taken from Perrin et al. (2006).

3.2.2. Shape and size of the dust grains

Astronomical dust grains probably have various shapes and structures (compact/fractal), as reflected in their different spectral signatures, which complicates the spectral analysis. Min et al. (2003, 2005) showed that mass absorption coefficients,

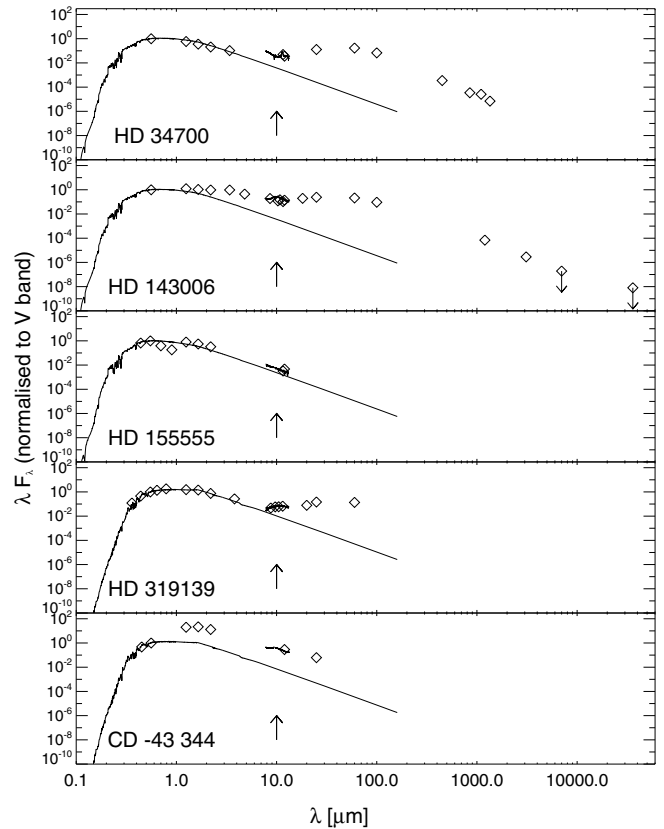


Fig. 2. The spectral energy distributions for the T Tauri stars. Remarkably, HD 155 555 shows no excess emission in the infrared.

calculated with a distribution of hollow spheres (DHS), provide a reliable identification of solid state components. In this work, we used mass absorption coefficients κ_i from van Boekel et al. (2005). More specifically, for the crystalline grains and silica, κ_i was calculated with DHS, while for the amorphous olivine and pyroxene grains, Mie theory was applied because here shape effects are less significant. For a more extensive discussion of shape and structure effects on spectral signatures, we refer to Min et al. (2003, 2005).

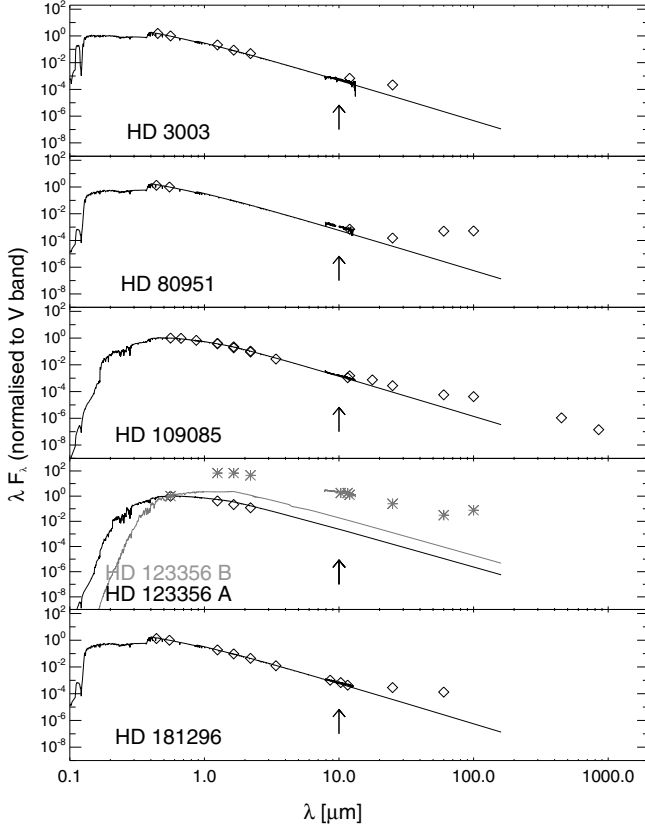


Fig. 3. Spectral energy distributions of the Vega-type stars. For the binary HD 123 356 the SED of the primary (*black curve*) is entirely stellar, while the excess emission is dominated by the secondary (*grey curve and stars*).

In circumstellar disks, dust grains grow and become destroyed by various processes. As a result, the dust grains do not have a single size, but a wide range in size. Since the grains are not always compact, but can be fluffy as well, the term “volume equivalent radius”, r_V is introduced, which is the radius of a sphere with the same material volume as the particle. This means that fluffy particles have a much smaller r_V than for their true size. Van Boekel et al. (2005) showed that the size distribution of grains radiating in the $10 \mu\text{m}$ region can be represented by two grain sizes: “small” ($r_V = 0.1 \mu\text{m}$) and “large” ($r_V = 1.5 \mu\text{m}$). It is this approach that we follow when modelling our spectra.

3.2.3. Fitting procedure

We used absorption coefficients from van Boekel et al. (2005) and Bouwman (2008), which are based on the laboratory data cited above. For the compositional fit, we perform an error analysis as described in Sect. 5.1.3 of van Boekel et al. (2005), by minimising the expression for the reduced χ^2

$$\chi_{\text{red}}^2 = \frac{1}{N_\lambda - M} \sum_{i=1}^{N_\lambda} \left| \frac{\mathcal{F}_v^{\text{model}}(\lambda_i) - \mathcal{F}_v^{\text{observed}}(\lambda_i)}{\sigma_i} \right|^2. \quad (1)$$

Since $\mathcal{F}_v^{\text{model}}$ contains 12 free parameters, i.e., the mass fractions of the five silicate emissivities for two grain sizes each and the continuum and dust temperature, M equals 12. The continuum temperature was determined by fitting a blackbody to the continuum. The number of wavelength points λ_i is N_λ , while σ_i describes the absolute error in the observed flux at wavelength λ_i and corresponds to the background noise derived from

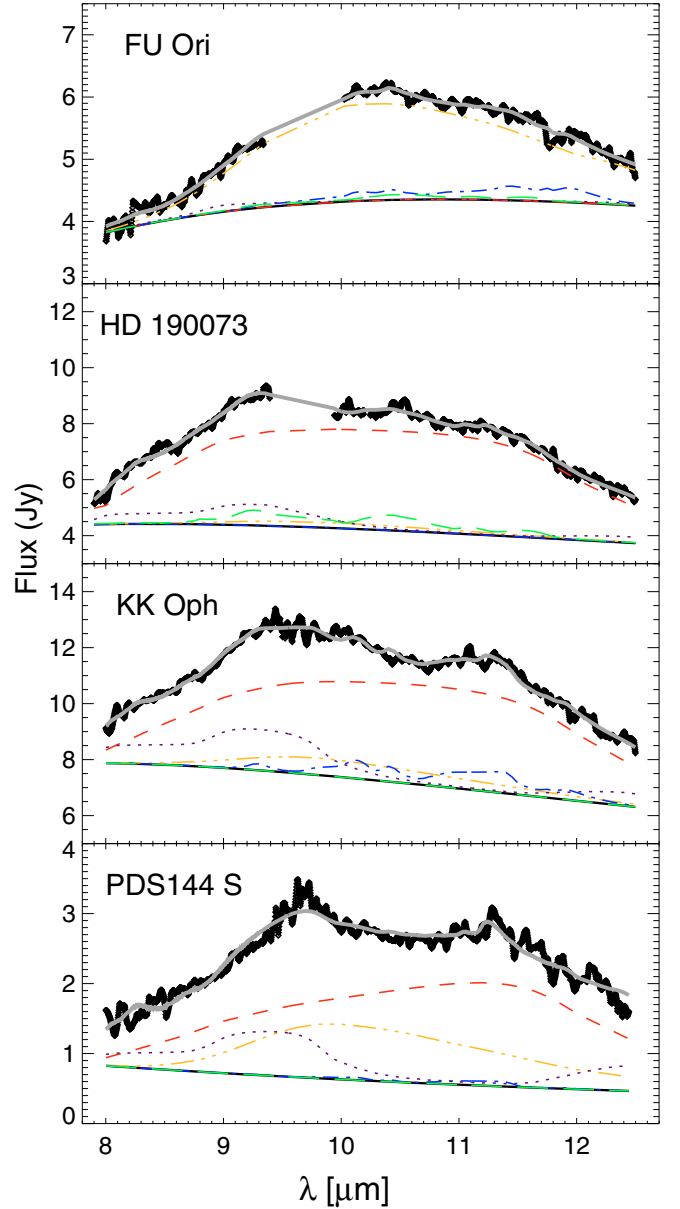


Fig. 4. Dust decomposition for FU Ori and the Herbig Ae stars. The different linestyles – or colours in the online version – represent small amorphous silicates (*dash-triple-dots, orange*), large amorphous silicates (*dashed, red*), both small and large grains of crystalline forsterite (*dash-dots, blue*), silica (SiO_2 , *dotted, purple*) and enstatite (*long curved dashes, green*). The very thick black curve corresponds to the observed spectrum. The sum of the different model components is given by the overplotted grey curve.

the data. The errors in the silicate mass fractions are derived from a Monte-Carlo simulation. For each spectrum, we create 100 synthetic spectra by randomly adding Gaussian noise with a width of up to the level of the background fluctuations at each wavelength point. The same compositional fitting procedure is applied to each of these spectra, resulting in slightly different mass fractions, from which the mean values and errors are obtained.

We caution against overinterpreting our fitting results. Significant systematic errors could indeed be introduced by either an imperfect calibration or the limited wavelength range and SNR, both inherent to ground-based observations (see Juhász et al. 2009 for a thorough discussion on this topic). Since we

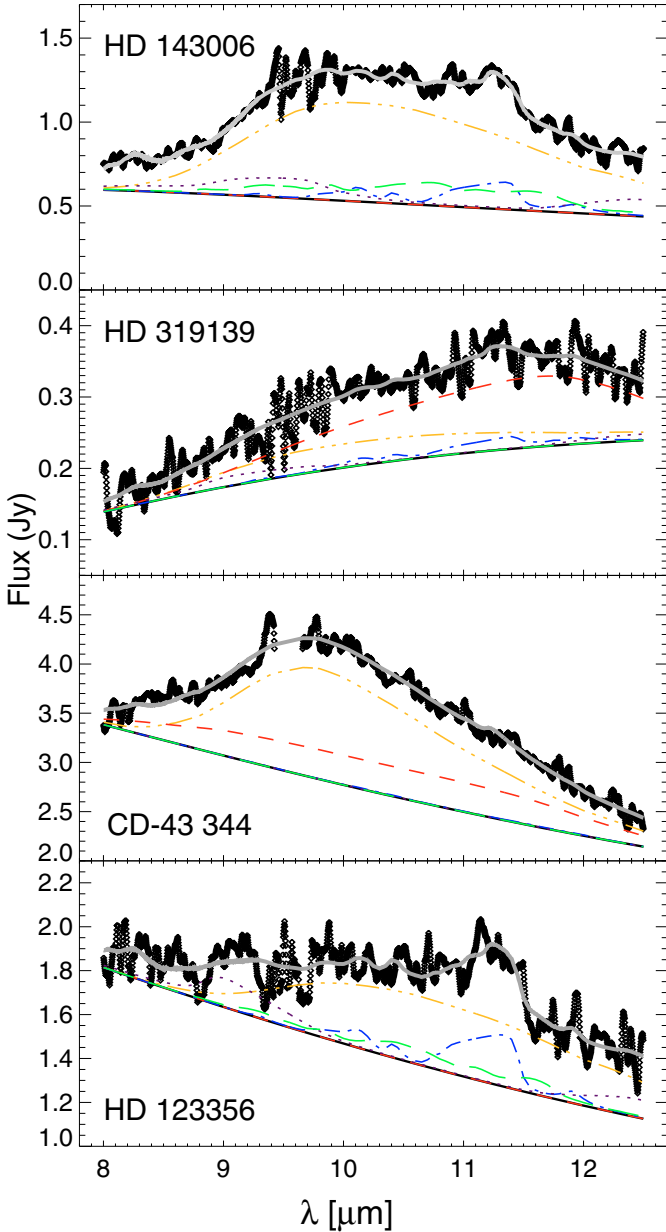


Fig. 5. Dust decomposition for the T Tauri stars (first three panels). See the caption of Fig. 4 for an explanation of the linestyles. *The bottom panel* shows HD 123 356, the only Vega-type object in our sample that shows a silicate feature.

cannot quantify these systematic errors, we were also unable to take them into account in the fitting procedure. Nevertheless, the results are capable of distinguishing between small and large grains, but probably only indicative for the crystalline species.

The modelling results for the emission spectra, and the contribution of each dust component are shown in Figs. 4–5. We note that, while we model the spectra with the 10 (grain and size) dust types and PAH as explained above, we plot only 6 components for clearer visibility. In particular, we added amorphous olivine and pyroxene at $0.1 \mu\text{m}$, plotting them as “small amorphous silicates”. Similarly, “large amorphous silicates” contain the $2.0 \mu\text{m}$ pyroxene and $2.0 \mu\text{m}$ olivine grains. For silica, forsterite, and enstatite, we plot the sum of the 0.1 and $2.0 \mu\text{m}$ grains.

When deriving the amount of the different dust species present, the linear coefficients of the fit – which are proportional to the radiating surface of the grains, assuming optically

thin emission – need to be converted into mass. However, it is not possible to determine the absolute amount of mass for each species present, since we have no spatially resolved data for deriving the particles’ size, density, or temperature distribution as a function of radius within the disk. Therefore, we derived mass fractions of the different species based on the assumptions that the particles (1) are spherical and (2) have the same density. The mass fractions are meaningful for comparing the objects in our sample and to establish the relative amount of processed dust that we observe at $10 \mu\text{m}$. In Table 3, we list the derived mass fractions, which is the ratio of the mass of a particular dust species to the total dust mass. We note that for a given mass, small particles have a larger total emitting surface than large ones. In contrast, a similar amount of observed radiation will result in a much smaller mass when caused by small grains than if caused by larger grains. We also note that our results are valid only for warm dust, which is located in the inner part of the disk atmosphere ($r < 10 \text{ AU}$) and radiates in the $10 \mu\text{m}$ region. If the disk atmosphere and midplane are well-mixed, the relative abundances should reflect the bulk composition of the inner disk, but if there is vertical settling the interpretation is more complex.

3.2.4. PAH

Polycyclic Aromatic Hydrocarbons (PAHs) show *N*-band emission features at 7.7 , 8.6 , 11.0 , 11.2 , and $12.7 \mu\text{m}$. A key result in observational studies of the PAH bands is that their profiles show clear variations in their peak positions, profile shape, and relative intensities (Peeters et al. 2004a and references therein). HII regions, reflection nebulae, and the ISM all exhibit the same PAH band profiles (called “class A”), while planetary nebulae and post-AGB stars have clearly different, red-shifted profiles, which are most noticeable for the 6.2 and $7.7 \mu\text{m}$ emission bands (class B/C). Figures 7 and 9 show these PAH profiles for two of our targets. We note that in contrast to class A, in which the PAH profiles in all objects are almost identical, class B comprises a wide variety of profiles for the 6.2 and $7.7 \mu\text{m}$ PAH bands (Peeters et al. 2002). The latter class is based on the spectra of evolved stars, where PAH formation and processing is actively taking place. HAeBe stars also exhibit large variations in their PAH profiles (Peeters et al. 2002; van Dienenhoven et al. 2004; Sloan et al. 2005). HAeBes with profiles similar to those found in the ISM (class A) are embedded in their parental cloud and PAHs from this cloud dominate the emission. Thus, the initial characteristics of the PAH family in the protoplanetary disks of HAeBe stars are the same as in the ISM. On the other hand, those HAeBes exhibiting significantly different PAH profiles (class B) are isolated HAeBe stars, and spatial studies show that their PAH emission originates in the disk (e.g. Habart et al. 2004, 2006; Geers et al. 2007b; Lagage et al. 2006; Doucet et al. 2007), implying that PAH processing is actively occurring in these disks. In addition, the presence of PAH emission is related to the disk geometry (Meeus et al. 2001; Acke & van den Ancker 2004): PAH emission is observed in flaring disks where the PAH molecules can be excited by UV photons from the central star, while it is much weaker (if present) in stars with a flat disk. A study of Spitzer-IRS observations of a sample of HAeBe stars and Post-AGB stars identified a correlation between the position of the 7.7 and $11.2 \mu\text{m}$ PAH bands and the effective temperature of the central star (Sloan et al. 2005, 2007).

PDS 144 N. Our TIMMI2 spectrum of PDS 144 N clearly shows PAH emission at 8.6 , 11.0 , and $11.2 \mu\text{m}$ (see Fig. 6).

Table 3. Relative mass fractions in percent derived from the model fits to the N -band spectra.

Object	Amorphous silicate		Forsterite		Silica		Enstatite	
	0.1 μm	2.0 μm	0.1 μm	2.0 μm	0.1 μm	2.0 μm	0.1 μm	2.0 μm
HD 123 356	76.0 ^{+1.3} _{-1.3}	0.0 ^{+0.2} _{-0.0}	7.0 ^{+0.5} _{-0.5}	...	11.4 ^{+0.3} _{-0.3}	...	4.6 ^{+0.7} _{-0.6}	1.0 ^{+1.0} _{-1.0}
HD 143 006	76.4 ^{+5.7} _{-4.0}	...	3.0 ^{+0.1} _{-0.2}	1.9 ^{+0.3} _{-0.6}	...	9.5 ^{+0.3} _{-0.7}	1.0 ^{+0.3} _{-0.2}	8.2 ^{+0.4} _{-1.3}
HD 190 073	3.7 ^{+0.5} _{-0.6}	85.3 ^{+0.3} _{-0.2}	7.2 ^{+0.1} _{-0.1}	3.9 ^{+0.1} _{-0.1}	...
HD 319 139	25.7 ^{+18.4} _{-17.0}	63.6 ^{+6.5} _{-6.8}	1.4 ^{+0.3} _{-0.4}	4.2 ^{+1.6} _{-1.7}	1.3 ^{+1.2} _{-1.1}	3.8 ^{+1.1} _{-1.0}
CD-43 344	74.3 ^{+0.7} _{-1.4}	24.8 ^{+0.9} _{-0.6}	...	0.9 ^{+0.7} _{-0.3}
FU Ori	87.9 ^{+5.6} _{-6.8}	...	0.3 ^{+0.2} _{-0.0}	9.0 ^{+0.7} _{-0.1}	1.4 ^{+0.2} _{-0.1}	...	1.4 ^{+0.2} _{-0.1}	...
KK Oph	9.7 ^{+0.8} _{-0.8}	70.3 ^{+9.3} _{-9.2}	2.1 ^{+0.1} _{-0.1}	6.1 ^{+0.4} _{-0.4}	...	11.8 ^{+0.2} _{-0.2}
PDS 144 S	30.7 ^{+1.4} _{-0.3}	54.6 ^{+0.4} _{-1.8}	0.5 ^{+0.2} _{-0.1}	14.2 ^{+0.3} _{-0.1}

“Amorphous silicates” indicate the sum of amorphous olivines and pyroxenes. Targets that do not show a silicate feature are not listed.

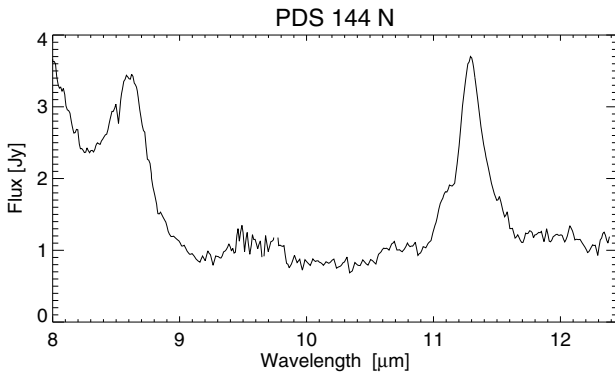


Fig. 6. The TIMMI2 spectrum of PDS 144 N, showing the 8.6, 11.0 and 11.2 μm PAH bands.

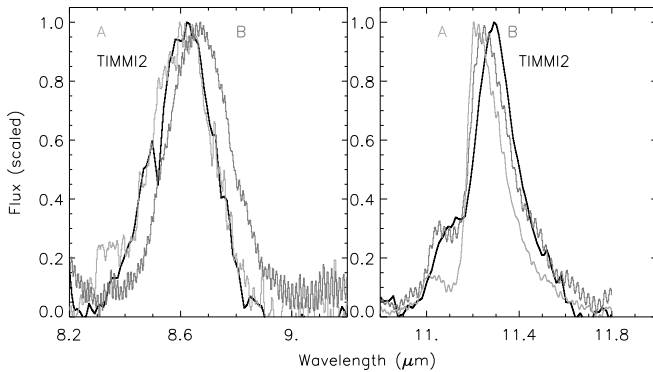


Fig. 7. A comparison of the 8.6 and 11.2 μm PAH band profiles of PDS 144 N (black) with the PAH classes (grey shades) as determined by Peeters et al. (2002) and van Diedenhoven et al. (2004). Clearly, PDS 144 N has a “class A” 8.6 μm PAH band, while the 11.2 μm PAH profile is different from both class A and B. The wavelength error is $\delta\lambda/\lambda \sim 10^{-3}$ for the science spectra, and $\delta\lambda/\lambda \sim 10^{-4}$ for the PAH class model profiles.

Comparison of the 8.6 and 11.2 μm PAH profiles with the different PAH classes (see Fig. 7) indicates that for PDS 144 N the 8.6 μm PAH band belongs to class A and hence is similar to the ISM. In contrast, its 11.2 μm PAH profile is distinct from both class A and B in that its peak wavelength is redshifted compared to both classes. Van Diedenhoven et al. (2004)

examined the 11.2 μm PAH band profile for a handful of HAeBe stars (other spectra were not adequate because of the presence of crystalline silicates at this wavelength or insufficient SNR). All but one of these stars belong to class A for all of their PAH bands. Sloan et al. (2005, 2007) reported class B characteristics for four HAeBe and a T Tauri star. In addition, these authors found a range of peak positions for the 11.2 μm band and related this to the effective temperature of the star, i.e., the central wavelength shifts to longer wavelengths as the effective temperature decreases. Tielens (2008) pointed out that this relationship can also be interpreted as a step function instead of a continuous dependence. In this respect, the deviation from class A seems to be connected to the presence of circumstellar material (Van Kerckhoven 2002; Boersma et al. 2008). However, the underlying cause of these variations in the 11.2 μm band is not well understood (see e.g., van Diedenhoven et al. 2004). For a “central wavelength” (the wavelength with half the emitted flux to either side, as defined by Sloan et al. 2007) of 11.289 μm and an effective temperature of 8750 K, this star supports this relationship (note that because of the asymmetry of the profile, the “central wavelength” does not correspond to the peak position). Given the class A 8.6 μm PAH emission, it seems that changes have affected the present PAH family in this source compared to that of the ISM and that these changes only seem to influence the 11.2 μm and not the 8.6 μm PAH bands. Observations of the CC modes (6.2 and “7.7” μm PAH bands, which are not observable from the ground) and a study of PAH emission in a larger sample of YSOs is needed to clarify this issue.

No N -band silicate emission is seen for the northern component, which can be explained if the silicate grains located in the inner parts of the disk are either (1) too cold, e.g., the disk lacks a hot optically thin surface, or (2) too large to emit at 10 μm , as shown by Meeus et al. (2002). Our spectrum with the prominent PAH features can be explained by a flared disk model (e.g., Acke & van den Ancker 2004), which is also clearly recognised in the resolved images by Perrin et al. (2006), who showed that the disk is optically thick in the NIR.

HD 34700. A comparison between our TIMMI2 observation and a Spitzer-IRS observation of HD 34700 is shown in Fig. 8, and clearly illustrates the presence of the 6.2, “7.7” and 11.2 μm PAH emission bands. A hint of the 8.6 and 12.7 μm PAH bands is also present in the Spitzer-IRS observations, while the weaker 12.0, 13.2, and 14.2 μm bands (e.g. Hony et al. 2001) and a

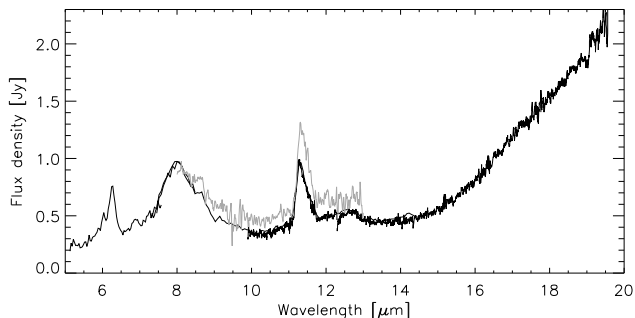


Fig. 8. TIMMI2 (grey) and Spitzer-IRS (thin black and thick black) observations of HD 34 700 are shown. PAH emission bands are clearly present on top of the dust continuum. Atmospheric variations may have influenced the spectrophotometric accuracy of the TIMMI2 data.

possible 15–20 μm PAH plateau/complex (e.g. Van Kerckhoven et al. 2000; Peeters et al. 2004b) are not observed in either spectrum.

A detailed comparison of the PAH band profiles is shown in Fig. 9. The PAH bands exhibited by the TTS HD 34 700 are clearly distinct. In particular, its 6.2 μm band peaks at a similar wavelength as that of the representative of class B, the Red Rectangle, but also shows excess emission shortwards of 6.1 μm and the long-wavelength tail is much weaker. A similar profile is observed towards the HAeBe star HD 141 569 (Sloan et al. 2005), both sources showing a very strong 6.0 μm PAH band (6.0/6.2 band ratio of ~ 0.33 and 0.42 for HD 141 569 and HD 34 700, respectively). Its “7.7” μm complex peaks around 8.05 μm , redshifted compared to the Red Rectangle but, as noted above, class B shows a large variety and other evolved stars such as, e.g. IRAS 17 347–3139, peak close to 8 μm . However, its profile is very broad, starting at similar wavelengths compared to that of the Red Rectangle, but extending up to 9 μm , thus it is more similar but blue-shifted to the class C profile. The latter class shows very weak, if any, 8.6 μm emission, which is also very weak in HD 34 700. Similar broad but unique PAH profiles are also seen around the HAeBe stars HD 141 569 and HD 135 344 (Sloan et al. 2005), suggesting a smooth transition in profiles between class B and C. The 11.2 μm PAH band in HD 34 700 peaks at a longer wavelength and also shows excess emission longwards, compared to the profile of the Red Rectangle. We note that the 11.0 μm PAH band, usually attributed to ionised PAHs (Hudgins & Allamandola 1999; Sloan et al. 1999; Hony et al. 2001), is not observed in HD 34 700. The TIMMI2 and Spitzer-IRS profiles are rather similar with only small differences in the blue wing of the 11.2 μm band. The “central wavelengths” (the wavelength with half the emitted flux on either side, as defined by Sloan et al. 2007) are 8.06, 11.35, and 11.37 μm for the 7.7 μm complex, the 11.2 μm band in the IRS-SH observations, and the 11.2 μm band in the TIMMI2 observations, respectively. While this is consistent with the results of Sloan et al. (2007) for the 11.2 μm band, the “central wavelength” of the 7.7 μm complex is considerably shorter for an effective temperature of 6000 K.

Summarising, the PAH band profiles of the T Tauri star HD 34 700 are clearly unique and indicate that PAH processing has occurred in this source. This is similar to PAH observations towards isolated HAeBe stars and a few other T Tauri stars and suggests that similar PAH processing occurs in protoplanetary disks around low-mass and intermediate-mass stars.

As for PDS 144 N, the absence of silicate emission in HD 34 700 can be explained if the silicate grains located in the

inner parts of the disk are either too cold or too large to emit at 10 μm . The shallow sub-mm slope of the SED in Fig. 2 suggests grain growth for those particles located in the outer disk and emitting at (sub-)mm wavelengths, but this does not necessarily imply the same evolution in the more inward disk regions. Although a far lower IR excess is seen in this SED, the prominent PAH emission suggests that the disk is still flared to some extent, and not self-shadowed. Alternatively, and taking into account that this system is a spectroscopic binary, the lack of warm dust could also be explained by an inner hole in a circumbinary disk, while the PAHs may be located further outwards and still emit at 10 μm .

4. Relations between stellar, disk, and silicate properties

We discuss the silicate shapes and study the silicate properties as a function of: (1) stellar luminosity, between ~ 0.5 and $\sim 500 L_{\odot}$; (2) binarity, with separations from approximately 0.1 to 5000 AU; and (3) infrared SED slope. To obtain more meaningful relations, we also consider the targets presented in Papers I and II. Apart from the three debris disks HD 113 766, HD 123 356, and HD 172 555, all other targets are PMS objects. We distinguish both disk types in the following discussion, when required.

4.1. Silicate shape as function of peak strength

The silicate mass fractions (Table 3) show no clear dependence on stellar parameters. As a function of age, we observe a decrease in amorphous silicates and an increase in crystalline forsterite and enstatite, in agreement with expectations, but no trend of grain growth with disk lifetime. To derive more robust conclusions, we use spectral indices because they are more robust and model independent. The silicate shape, i.e., the ratio of the flux at 11.3 to that at 9.8 μm in the continuum normalised spectra, constitutes a good probe to study trends and correlations, and can be seen as a direct indicator of the grain size (Bouwman et al. 2001; van Boekel et al. 2003).

The silicate shape as a function of the peak strength is shown in Fig. 10. To compare our results with previous studies, we follow the same definition of the silicate peak strength and shape as given in Sect. 4.2 of van Boekel et al. (2005). In a weighted linear fit with relation $y = a + bx$, where x is the feature strength and y the flux ratio, values of b between $-0.28 \leq b \leq -0.16$ have been reported (van Boekel et al. 2003; Przygodda et al. 2003; Kessler-Silacci et al. 2007). We cannot present a mathematical relation for our sample, because it lacks sources of very pristine dust (which would populate the middle bottom in Fig. 10). To compare with a larger sample, we added data from Sicilia-Aguilar et al. (2007). The Vega-type HD 113 766 (label number “3”) has an isolated position in our plot, because of its second generation dust and its double peak in the spectrum. Besides this object, our sample of PMS disks agrees qualitatively well with the correlations found in the cited works: a decrease in the peak strength correlates with an increase in the dust processing (i.e., with a higher 11.3/9.8 ratio).

4.2. Grain processing as a function of stellar luminosity

No correlation of the crystalline mass fractions (Table 3) with either stellar luminosity or derived grain size is found in our sample. Kessler-Silacci et al. (2007) identified a correlation of the

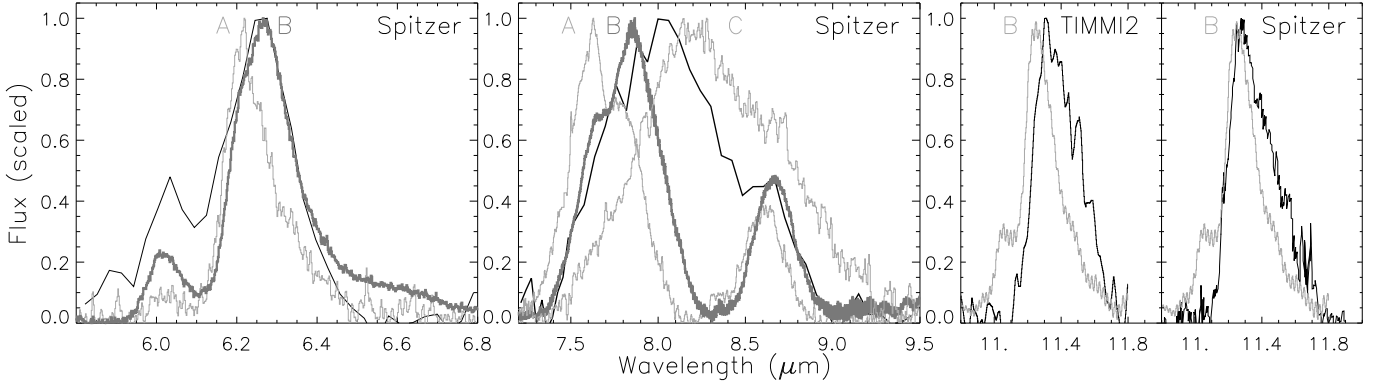


Fig. 9. A comparison of the 6.2, “7.7”, 8.6 and 11.2 μm PAH band profiles of HD 34700 with the PAH classes as determined by Peeters et al. (2002) and van Dienenhoven et al. (2004). Observations of HD 34700 are shown in thin black (both Spitzer-IRS and TIMMI2), the PAH classes are shown in grey shades. Clearly, HD 34700 shows unique PAH band profiles. Errors are given in the caption of Fig. 7.

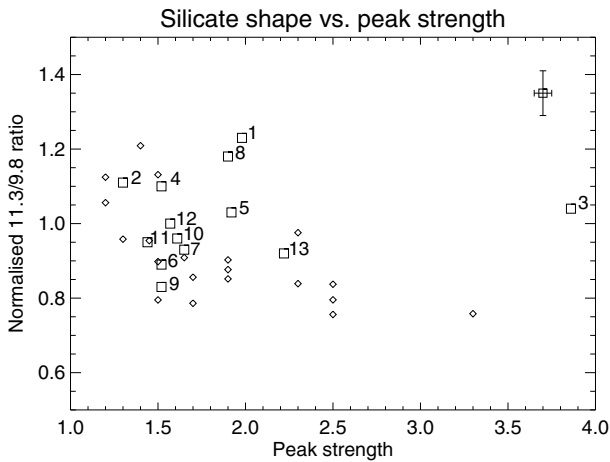


Fig. 10. Silicate shape (the 11.3/9.8 ratio) as a function of peak strength. While HD 113 766 (data point “3”) is distinctive because of its secondary generation dust, and sources of very pristine dust are missing in our sample, the data follow the same trend as found in previous studies. The target number labels are explained in Table 4. Typical error bars are given in the top right corner. For comparison, data from Sicilia-Aguilar et al. (2007) is included (small diamonds).

silicate shape with stellar luminosity, in the form of an observed larger grain size (as inferred by the 11.3/9.8 ratio) with lower luminosity. This trend can be understood by considering that the 10 μm silicate emission region lies further inward for stars with lower luminosity, assuming that the grain size distribution with radius is the same in all disks, and grain growth is most efficient in the inner, denser regions. Our sample is much smaller than that presented by Kessler-Silacci et al. (2007), and we cannot give a mathematical relation because of the scatter in our data points, but Fig. 11 suggests a similar trend with luminosity.

4.3. Influence of companions

We see no correlation of the degree of dust processing with stellar binarity in our sample, i.e., whether the time spans of dust processing and disk lifetime in binary systems would differ from those of isolated stars of the same age. Binaries or multiple systems represent 75% of our targets. These include systems without *N*-band silicate emission (e.g., HD 3003, HD 80951, HD 155555, HD 181296), objects with mainly unprocessed dust (FU Ori) or large dust grains (KK Oph,

Table 4. Labels and luminosities (with errors when they were given in the literature) used in Figs. 10–12.

Label	Target	L/L_{\odot}	Ref.
1	HD 72 106 B	$9.9^{+12.7}_{-5.6}$	(1)
2	HD 98 800 B	$0.58^{+0.11}_{-0.11}$	(2)
3	HD 113 766 A	$4.4^{+0.4}_{-0.4}$	(3)
4	HD 123 356 B	...	(4)
5	HD 143 006	0.8	(5)
6	HD 172 555	>16	(6)
7	HD 190 073	83	(7)
8	HD 319 139	$0.49^{+0.06}_{-0.06} + 0.33^{+0.04}_{-0.04}$	(8)
9	CD-43 344	...	(9)
10	FU Ori A	466	(10)
11	KK Oph A	20^{+5}_{-4}	(11)
12	MP Mus	>0.45	(6)
13	PDS 144 S	>16	(6)

References: (1) Folsom et al. (2007), (2) Prato et al. (2001), (3) Lisse et al. (2008), (4) neither distance nor the spectral type are certain, (5) Natta et al. (2004), (6) lower limit when assuming a ZAMS luminosity for the given spectral types, (7) Acke et al. (2005), (8) Quast et al. (2000), (9) no luminosity class is known, (10) Green et al. (2006), (11) adapted by Carmona et al. (2007).

HD 319 139), and sources with all types of silicates present (especially HD 123 356).

For most binaries in our sample, the separation (cf. Table 1) is around 200 AU (apart from PDS 144 with ~ 5000 AU), while dust in very different processing stages is found. In case of the three spectroscopic binary (SB) systems, silicate dust is either seen in small amounts or is absent, which can be explained by the removal of dust inside the circumbinary disk. Pascucci et al. (2008) demonstrated that companions at separations of tens of AU have no impact on the dust evolution, which would be interesting to study for a carefully defined target sample with closer companions.

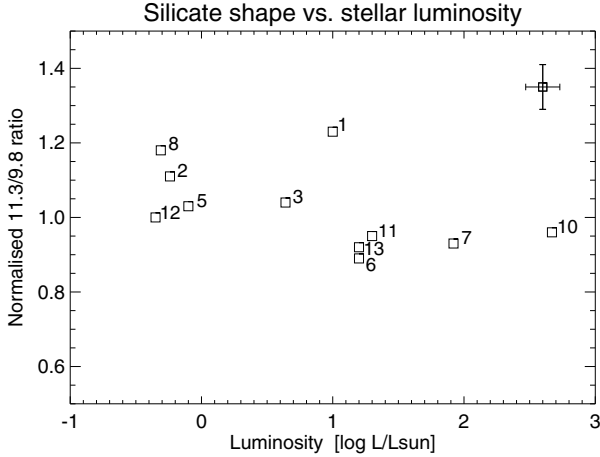


Fig. 11. Silicate shape as a function of stellar luminosity. Objects with uncertain luminosity are excluded in this plot. Typical error bars are shown in the top right corner. The luminosities are listed in Table 4.

4.4. Silicate strength as a function of SED slope

With ongoing grain growth and subsequent settling, an initially flared PMS disk is understood to evolve into a flat disk (Dullemond & Dominik 2004), accompanied by a change in the slope of the SED, i.e., the initially positive 2–25 μm slope will decrease. During the evolution into a debris disk, the IR emission from the inner disk decreases when the disk is cleared from the inside out. This results in a steeper negative SED slope with progressive evolution into a debris disk. When the dust has nearly completely disappeared, the slope will approach that of a blackbody with the stellar temperature. A dependence of silicate emission on inner disk evolution would be recognisable as a correlation between silicate strength and SED slope. There is a tendency for more flared (and therefore redder) disks to have stronger silicate features. We used an average extinction curve (Savage & Mathis 1979) for $R = 3.1$ and the values of A_v given in Table 1 to calculate the dereddening of the SEDs. The slope between 2–25 μm was calculated as

$$\alpha_{2-25} = \frac{\log F_{25} - \log F_2}{\log \lambda_{25} - \log \lambda_2}, \quad (2)$$

where F is the flux in Jansky at the indicated wavelengths. Sicilia-Aguilar et al. (2007) noticed a very weak to absent correlation between silicate strength and SED slope, with which our data agree (see Fig. 12). Vega-type and pre-main sequence stars can be clearly distinguished by their different slopes, but a convincing dependence on the silicate strength is not seen. In this plot, CD-43 344 has an unusual position for a PMS source, but as noted earlier, its classification is not certain.

5. Discussion

We have presented new N -band spectra of 15 PMS and Vega-type stars. Besides FU Ori, these spectra were either previously unpublished or not yet available in a high quality to permit the analysis of the PAH bands or a dust decomposition of the silicate emission. HD 155 555 AB is the only T Tauri star in our sample without an IR excess, while four of the five Vega-like stars only show photospheric emission at 10 μm , with excess emission only at longer wavelengths. For the remaining targets, we analysed

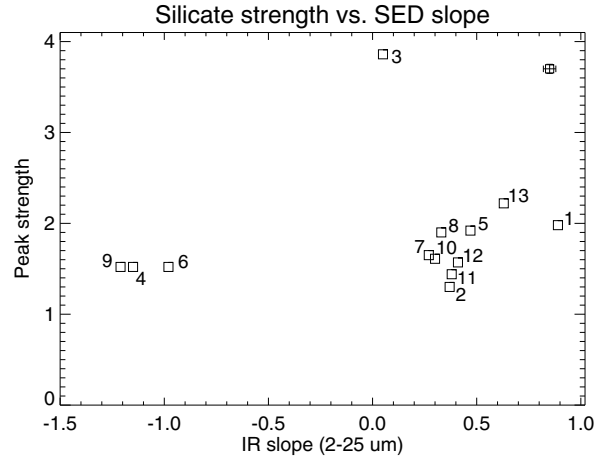


Fig. 12. Silicate peak strength versus infrared 2–25 μm SED slope ($d \log F_\lambda / d \log \lambda$). HD 113 766 (data point “3”) has a particular position due to its large amounts of secondary generation dust. See Table 4 for the number labels. Typical error bars are plotted in the top right corner.

their silicate and PAH features:

- **Silicate dust.** Unprocessed dust dominates the circumstellar matter around FU Ori, HD 123 356, HD 143 006 and CD-43 344. HD 123 356 is considered to be a Vega-type object, and we show for the first time that the dust emission originates from its secondary. No firm age estimation is available and we do not exclude the possibility that this system may be younger than currently believed. The N -band profile of HD 123 356 B is rather unusual, dominated by small amorphous silicates with all types of processed dust being present. High-resolution NIR and MIR studies are required to learn more about this system. Similarly, the classification of CD-43 344 as a T Tauri star remains ambiguous. No distance, luminosity class, or age estimation is available. Its dust properties could also be explained by it being an evolved Mira-type star. Optical spectroscopy is required to determine the stellar class.

Large amorphous silicates are the main dust component towards HD 190 073, HD 319 139, KK Oph, and PDS 144 S. No source in our sample shows the presence of highly processed dust, i.e., a spectrum dominated by crystalline silicates, as we found for some targets presented in Paper I and II (e.g., the Herbig Ae star HD 72 106 B or the Vega-type HD 113 766 A). In agreement with previous studies, we found no correlation of dust processing with stellar age in our samples. Although HD 181 296 and HD 172 555 have a similar age and spectral type, the first source has no excess emission in the N -band, while the last, presented in Paper II, shows dust in an early stage of processing. This could be explained by a cleared inner disk region of different sizes, where the disk region sensitive to N -band observations (<10 AU) has already been cleared in HD 181 296.

We see no correlation between the dust evolution and binarity in our sample, i.e., whether the dust processing in binary systems is retarded or accelerated in relation to isolated stars.

- **PAH emission.** PAH bands are observed towards the HAeBe star PDS 144 N and the TTS HD 34 700. Their presence is often observed in HAeBe stars and commonly explained with the excitation of PAH molecules by UV photons. However, Li & Draine (2002) demonstrated that PAH

molecules around cool stars can also be excited. Laboratory experiments by Mattioda et al. (2005) detected electronic absorption bands of PAH ions up to the NIR. Thus, PAH emission can also be found in UV-poor environments. In 5–35 μm spectra of a sample of 38 TTS, Geers et al. (2006) found PAHs for 3 targets (with possible further tentative detections). In their sample, T Cha of spectral type G8 represents the lowest mass source with PAH emission. Furlan et al. (2006) found 2 cool stars with PAH emission in 5–36 μm spectra of 111 targets in the Taurus-Auriga star-forming region. They show UX Tau A as the coolest TTS with PAH until now, of spectral type K5, but the PAH feature in this source is rather marginal. The latest-type PAH-emitting TTS found to date is IRS 48, studied by Geers et al. (2007a), who emphasise that its apparent spectral type (M0) has varied significantly in the past decade, possibly because of a FUOR-type accretion event.

The PAH profiles of HD 34 700 show that PAH processing occurs in a similar way to PAHs observed towards isolated HAeBe stars, suggesting that similar PAH processing exists in the protoplanetary disks around low-mass and intermediate-mass stars. The case is less clear for the HAeBe star PDS 144 N. Although the 8.6 μm PAH band profile is identical to that in the ISM, the 11.2 μm PAH band is clearly distinct.

PDS 144 constitutes a very interesting system, which has prominent PAH bands towards the Northern source, while the Southern component is dominated by silicate emission. Although it is commonly believed that both objects form a binary, this remains to be proven. Perrin et al. (private communication) obtained optical spectra to determine more accurate spectral types and an improved distance estimate, and attempt to provide a more robust answer to this question.

6. Conclusions

We have presented new *N*-band spectroscopy of 15 PMS and Vega-type stars, and modelled the 10 μm emission features, to characterise the circumstellar dust in each object of our sample. We also discovered previously unknown circumstellar disks. Our main conclusions are:

1. We characterised the PAH emission in PDS 144 N and HD 34 700. PDS 144 N exhibits mixed PAH class characteristics, while HD 34 700 clearly belongs to class B. The latter points towards processing of PAHs, suggesting a similar PAH evolution in the disks of Herbig and T Tauri stars.
2. The emission spectrum of FU Ori resembles that of BBW 76 in Paper I, while the FUORs V346 Nor, V883 Ori and Z CMa of Paper I show silicate absorption features. This could be an effect of the disk orientation (pole-on vs. face-on) or represent the two FUOR categories defined by Quanz et al. (2007).
3. We showed the first *N*-band spectrum of CD-43 344, a star that hosts only pristine silicates and had been poorly studied. However, its luminosity and stellar class remain uncertain.
4. Silicate dust with mixed properties (sizes and crystallinity) is found towards HD 123 356 B, while high-resolution imaging is required to achieve a deeper understanding of this particular system.
5. Within our sensitivities, no *N*-band silicate emission is seen for the T Tauri star HD 155 555 AB and the Vega-type objects η Corvi, HD 3003, HD 80 951, and HD 181 296.
6. We failed to detect HD 158 153 and SAO 185 668, despite their alleged high IRAS flux and the sufficient integration times of their data. We attribute this to other sources being present in the IRAS beam, causing erroneous fluxes for our target. There are many other stars for which an IRAS flux had been measured in the 1990s, but these measurements were later revised, when higher spatial resolution became possible in the IR.
7. We find no dependence of dust processing on either age or stellar binarity, for a companion separation of typically >100 AU.

Acknowledgements. G.M. acknowledges financial support by the Deutsche Forschungsgemeinschaft (DFG) under grants ME2061/3-1 and /3-2. We would like to thank Alexis Brandeker for the analysis and discussion of the photometric VISIR data of η Corvi, and Aurora Sicilia-Aguilar for providing the additional data plotted in Fig. 10. This work made use of the SIMBAD astronomical database. We thank the La Silla staff and telescope operators for support during the observations.

Appendix A: Comments on individual sources

A.1. FU Ori stars

FU Orionis objects (FUORs) show a variability characterised by dramatic outbursts in optical light, followed by a fading phase that can last decades. The origin of this phenomenon is not clear but it is often associated with enhanced accretion in low-mass pre-main sequence stars (Hartmann & Kenyon 1996).

FU Ori is the prototype of the FU Orionis phenomenon. While the SIMBAD database lists a spectral type of G3Iavar, Kenyon et al. (2000) changed it to G0II. In contrast to Hanner et al. (1998), who measured an increasing MIR flux shortward of 10 μm , the spectra of Schegerer et al. (2006) and Quanz et al. (2006) agree very well with ours, indicating that this object was not variable in the MIR between Dec. 2002 and Jan. 2006 (or at least that any period of variability was not observed). No Kurucz model was plotted in the SED of FU Ori as explained in Sect. 3.1, but it is recognisable that the total IR excess of this source is larger than for all other targets in this work. The analysis of the silicate emission feature shows that it is dominated by small amorphous silicates. Besides some forsterite, no other dust species is found for this target in substantial amounts.

Compared to the four FUOR spectra shown in Paper I, we see that FU Ori agrees well with the spectral profile of BBW 76, while the other 3 FUORs V346 Nor, V883 Ori, and Z CMa exhibit very different profiles because they are in absorption. The appearance of FUOR MIR spectra could be a geometrical effect: pole-on (emission feature) versus edge-on (absorption feature) view of the disk. However, given the large number of FUORs with silicate absorption features, this difference cannot be explained by disk orientation alone. Therefore, Quanz et al. (2007) defined two categories of FUORs: (1) objects for which the silicate feature is in absorption probably remain embedded in a circumstellar envelope; and (2) objects where the silicate band is in emission, which are understood to have largely shed their envelope, and the feature arises in the surface layer of their accretion disks.

A.2. Herbig Ae/Be objects

HD 190073 has been discussed in the literature for more than 70 years and had various classifications. Being previously

considered a post-main sequence giant, van den Ancker et al. (1998) described HD 190 073 as a Herbig Ae/Be star, which is now generally accepted. Considering its large distance, for which only a lower limit is known due to an imprecise Hipparcos parallax (van den Ancker et al. 1998), this unusual object must be far more luminous than other Herbig stars of similar spectral type. The optical spectrum is also quite peculiar (Pogodin et al. 2005).

The SED shows an IR excess that begins in the NIR and rises to the far-IR. The decomposition of the *N*-band silicate feature shows a strong dominance of large amorphous silicates. Silica and enstatite are present in much smaller amounts, while no forsterite is found.

KK Oph is a PMS binary with a 1.6'' separation (e.g. Leinert et al. 1997) that shows brightness variations typical of the UX Orionis type (it reddens when becoming fainter). Controversial spectral types have been determined (between Be and F0) and the system was repeatedly suggested to constitute a Herbig Ae star with a K-type classical T Tauri companion (e.g. Leinert et al. 1997; Hernandez et al. 2004; Herbig 2005). Carmona et al. (2007) derived a spectral type A6Ve for the primary and G6Ve for the companion. Various estimates place this target at a distance between 160 and 310 pc, the lower limit being most frequently cited.

The *N*-band spectrum discussed here was already shown in Leinert et al. (2004), but the silicate feature had not yet been analysed in terms of dust composition. In the TIMMI2 images, we see one isolated source, most likely just the HAe star itself, but we note that the MIR sensitivities were not good during that night. The ESO/ST-ECF Science Archive contains another TIMMI2 spectrum of KK Oph, which is described in Geers et al. (2005). These two spectra differ by about 10% in the 8 μm flux, while being in agreement longward of 10 μm . Both spectra, as well as the standard stars, were observed at an airmass close to 1.0. The distance in time between object and closest standard star was approximately one hour in both cases. We selected the first mentioned spectrum, since it matches more closely the TIMMI2 N1 photometry from the Science Archive.

The decomposition into dust components illustrates its diverse composition. Large amorphous silicates dominate, but silica and forsterite are also found in significant amounts, while enstatite is not detected.

PDS 144 N. During the Pico dos Dias Survey, Torres et al. (1995) discovered the binarity of this Herbig Ae/Be star with a 5'' separation. Spectral types of both components, given in Table 1, were determined by Vieira et al. (2003). Perrin et al. (2006) presented comprehensive multiwavelength observations and discussed the possible distance to PDS 144, proposing a value of 1000 ± 200 pc, while previous estimates gave $d = 140\text{--}2000$ pc. Although it is commonly believed that both stars form a binary system, this has not yet been explicitly proven. The dominance of PAHs in PDS 144 N can be recognised from the NIR images in Perrin et al. (2006), showing an optically thick, edge-on flared disk, where the emission in the 3.3 μm band clearly stands out in intensity. Until now, *N*-band spectra of both components have not yet been published.

PDS 144 S. Resolved circumstellar emission from the more luminous component PDS 144 S was not detected in our and

previous *N*-band images, but had been found by Perrin et al. (private communication) at 18 μm (0.57'' diameter). In the *N*-band spectrum, we see silicate features of mainly large amorphous silicate grains, in addition to small amorphous grains and silica. Forsterite and enstatite are absent, which is indicative of unprocessed dust, while small amounts of PAHs might be present as well. We note that our spectrum was taken during a night with strong variations in the MIR transparency, but great care was taken in its calibration by applying a close standard star at similar airmass observed immediately after the science exposure.

Both components of PDS 144 have a similar spectral type and, assuming that they formed together, a similar age, but show different emission features, PAH compared to silicates. The presence/absence of PAH bands could be explained by the disk geometry, since we would observe far lower amounts of PAH emission from a flat, self-shadowed disk, which prevents the UV photons from reaching the PAH molecules (e.g. Dullemond & Dominik 2004). On the other hand, we do not want to exclude the trivial explanation that the amounts of PAH in both disks could be different, despite the similarity of both sources.

A.3. T Tauri targets

HD 34 700 constitutes a quadruple T Tauri system. For the inner, short-period ($P \sim 23.5$ days) spectroscopic binary, Torres (2004) had performed an orbital solution and showed that both stars are of similar mass and luminosity. Sterzik et al. (2005) found two more, faint, late-type components of PMS nature. Despite several indicators of stellar youth (IR excess, X-ray emission, H α emission), the precise age has not yet been established, since the Hipparcos parallax is very uncertain (0.86 ± 1.84 mas).

Sub-mm observations of HD 34 700 were reported by, e.g., Sylvester et al. (2001) and Sheret et al. (2004). An *N*-band spectrum was shown in Sylvester & Mannings (2000), but its low SNR did not permit a detailed study. Our TIMMI2 spectrum is also of higher quality than the ISO-SWS and ISO-PHOT data of Acke & van den Ancker (2004). As can be seen from the Kurucz model, excess emission starts around 5 μm and becomes dominant at MIR to mm wavelengths. A PAH band feature at 3.3 μm was shown by Smith et al. (2004).

HD 143 006. As for several other PMS objects, this star was also previously erroneously classified as a pre-planetary nebula, but now is commonly considered to be a TTS (see, e.g., Mamajek et al. 2004). In contrast to the assumption of a disk-like distribution of the circumstellar dust, Dent et al. (2005) found single-peaked, narrow CO lines, which are more consistent with emission from an envelope rather than a disk.

Our SED shows a large NIR excess attributable to hot dust emission. Such a large NIR excess is often associated with polarised emission from the circumstellar matter (Yudin 2000), but Hales et al. (2006) did not find any polarised emission and concluded that the disk may be too small to be resolved in their UKIRT observations.

The decomposition of the *N*-band spectrum shows evidence of dust at a very early stage of processing. Small amorphous silicate grains dominate the *N*-band feature, and there are smaller amounts of silica, enstatite, and forsterite. Moderate PAH emission is seen on top of the silicate feature, causing small peaks in the spectrum between 8–9 μm and at 11.2 μm .

HD 155 555 (alias V824 Arae) is a member of the β Pic moving group (Torres et al. 2006) and consists of a G5IV star in a short-period orbit ($P \sim 1.68$ days) with a K0IV-V spectroscopic companion (e.g., Strassmeier & Rice 2000). Another M4.5 visual companion is located $33''$ away. The system had been considered to be a RS CVn type, however, Pasquini et al. (1991) proposed it to be a TTS. Both classifications are still being used. A single source is seen in our TIMMI2 images, while we were pointing at the positions of the A and B components. The C component was just outside the field of view, which explains why IRAS obtained a higher $12 \mu\text{m}$ flux than observed in our data. Within our sample of T Tauri stars, HD 155 555 AB constitutes the only target without detected excess emission above the stellar photosphere.

HD 319 139. The spectroscopic binary TTS and member of the β Pic moving group (Torres et al. 2006) HD 319 139 (alias V4046 Sgr) has been known to be an emission-line star since the year 1938. For a summary of its “early history” see, e.g., Byrne (1986). Hutchinson et al. (1990) performed photometry from the UV to the mid-IR Q -band. From the absence of a NIR excess, Jensen & Mathieu (1997) concluded that there is an inner hole in its circumbinary disk. Quast et al. (2000) refined the orbital period to 2.421 days and determined the spectral types of both components to K5Ve and K7Ve. All the afore mentioned authors provided distance estimates in the range 42–83 pc. In this work, we assume 83 pc (Quast et al. 2000), since this is the most recent estimate.

Our N11.9 flux (central wavelength $11.6 \mu\text{m}$) of HD 319 139 is about 20% below the corresponding IRAS flux, but it matches the $11.5 \mu\text{m}$ flux determined by Hutchinson et al. (1990) very well. We see a rising dust continuum, on top of which large amorphous silicates dominate the emission feature, in addition to small amorphous grains and some forsterite and silica. The N -band spectrum published by Honda et al. (2006), who observed a sample of 30 low-mass stars with COMICS at the Subaru Telescope, agrees with our data.

CD-43 344. Mannings & Barlow (1998) proposed that the F6V star HD 7151 is a debris disk candidate, by cross-correlating the “Michigan Catalog of Two-dimensional Spectral Types for the HD Stars” with the “IRAS Faint Source Survey Catalog”, and associated IRAS F01089-4257 with this star. Sylvester & Mannings (2000), however, showed that the more closely located M2 star CPD-43 142, primarily known as CD-43 344, could explain the emission of this IRAS FSC source more precisely. Despite a significant MIR excess, this object was not targeted by previous studies. Here we consider this target to be a TTS, based on its spectral type and pristine status of dust processing, but this classification is not a unique solution since, e.g., an evolved Mira-type star could show the same dust emission. Currently the distance to CD-43 344 and its luminosity class are undetermined.

The 2MASS fluxes in the SED might be influenced by other sources, since the attributed NIR excess seems extraordinarily high. In the MIR, however, the target appears isolated. The decomposition of the silicate emission feature is dominated by small amorphous silicates with a less prominent contribution of larger grains. We did not find evidence of crystalline dust.

A.4. Vega-type stars

HD 3003 is a proposed member of the Tucana/Horologium Association (Zuckerman & Song 2004). In the “Catalog of

Components of Double & Multiple stars” (Dommanget & Nys 2002), it is listed as a binary system with $0.1''$ separation and almost equal visual brightness of the components. Since this measurement is listed as being obtained in 1925, we interpret this information with care. In our TIMMI2 data (with $\sim 0.2''$ pixel resolution), only one isolated point-like emission source is seen. Song et al. (2001) estimated an age of 50 Myr with an upper limit of 247 Myr. The SED for this target shows no IR excess emission up to the N -band, with little excess seen at $25 \mu\text{m}$.

HD 80 951 constitutes a quadruple system (Dommanget & Nys 2002). Oudmaijer et al. (1992), as well as Mannings & Barlow (1998) characterised it as a system with excess emission in the IRAS passbands, but no further indication of circumstellar matter has been described in the literature. Our TIMMI2 N -band spectrum is consistent with the presence of photospheric emission. From the SED, we see an IR excess starting around $25 \mu\text{m}$.

HD 109 085. Stencel & Backman (1991) and later Mannings & Barlow (1998) characterised HD 109 085 (alias η Corvi) as a Vega-type object. At $850 \mu\text{m}$, a disk is found and resolved with a size of ~ 100 AU (Wyatt et al. 2005). As shown by the SED of this target, excess emission is insignificant at $10 \mu\text{m}$ and starts longward of $\sim 17 \mu\text{m}$, extending into the sub-mm regime. Our TIMMI2 N -band spectrum appears stellar. In Spitzer IRS data, Chen et al. (2006) detected a faint silicate feature around $10 \mu\text{m}$.

HD 123 356. There is not much information about HD 123 356. In “The Washington Visual Double Star Catalog” (Worley & Douglass 1997), it is listed as having a companion 2.2 mag fainter in V -band, separated by $2.5''$ at a position angle of 126° . Mannings & Barlow (1998) identified HD 123 356 as a candidate main-sequence debris disk object, by cross-correlating the “Michigan Catalog of Two-dimensional Spectral Types for the HD Stars” with the “IRAS Faint Source Survey Catalog”. Sylvester et al. (2000) presented a moderate-SNR N -band spectrum, which appeared quite different from ours. The authors, however, clarified that their CGS3 beam of $5.5''$ was pointing at the position of the primary (the secondary being at the edge of the beam) and that not all of the IR signal would have been detected if a substantial part of the emission originates from the secondary. No significant CO emission (Dent et al. 2005) and only a very small amount of NIR polarimetric emission (Hales et al. 2006) was found.

Compared to the other emission feature sources, the TIMMI2 N -band spectrum of HD 123 356 appears atypical, since the flux remains rather constant between 8 and $11 \mu\text{m}$. However, our N -band spectra were acquired in three separate observing runs (March 2003, February 2005 and January 2006), always exhibiting the same spectral shape. From the modelling of the circumstellar emission, the dust seems to be at a rather early processing stage (or mainly unprocessed). As shown in Fig. 5, the emission is dominated by small amorphous silicates, in addition to small amounts of forsterite, silica, enstatite, and PAH.

While the currently available data of HD 123 356 are consistent with it being a Vega-type star and circumstellar dust in a retarded stage of processing, the true nature of this system can only be revealed with high-resolution NIR- and MIR-observations.

HD 181 296. Mannings & Barlow (1998) identified HD 181 296 (alias HR 7329, or η Tel) as a Vega-like star.

A brown dwarf companion at a projected distance of 200 AU was found by Lowrance et al. (2000). This target is also part of the β Pic moving group (Torres et al. 2006).

From our TIMM12 N1 photometry at central wavelength $8.6 \mu\text{m}$, the reported $12 \mu\text{m}$ IRAS flux appears overestimated, while our photometry and N -band spectral profile are in excellent agreement with the fluxes that Mamajek et al. (2004) reported for $10.3 \mu\text{m}$ and $11.6 \mu\text{m}$.

A.5. Non-detections

Two objects for which a significant MIR flux was reported by IRAS remain undetected in our observations, although the stated fluxes should have been easily observable. This was probably caused by other sources being inside the large IRAS beam. We report these non-detections to clarify the situation for these targets in the literature.

HD 158 153. In the SIMBAD database, an IRAS flux of 3.83 Jy at $12 \mu\text{m}$ is given. This source was also mentioned in the work by Oudmaijer et al. (1992). With a 10σ sensitivity of 25 mJy/h, we did not detect a source at this position within 3 min of integration time, suggesting a flux limit <110 mJy. Several IRAS sources are located nearby, of which the $11''$ close object IRAS 17251–2320 seems to emit the highest flux. We find an increasing dust continuum for that source, but do not present this in detail here, since its nature (stellar or not) remains unclear.

SAO 185 668 is listed in SIMBAD with an IRAS flux of 1.61 Jy at $12 \mu\text{m}$. Malfait et al. (1998) considered it to be a Vega-like star based on its IRAS photometry. For data with a poor 10σ MIR sensitivity around 100–150 mJy/h, no signal was found within 12 min of on-source time, resulting in a flux limit of about <0.3 Jy.

References

- Acke, B., & van den Ancker, M. E. 2004, *A&A*, 426, 151
 Acke, B., van den Ancker, M. E., & Dullemond, C. P. 2005, *A&A*, 436, 209
 Beichman, C. A., Bryden, G., Gautier, T. N., et al. 2005, *ApJ*, 626, 1061
 Boersma, C., Bouwman, J., Lahuis, F., et al. 2008, *A&A*, 484, 241
 Bouwman, J., Meeus, G., de Koter, A., et al. 2001, *A&A*, 375, 950
 Bouwman, J., Henning, Th., Hillenbrand, L. A., et al. 2008, *ApJ*, 683, 479
 Byrne, P. B. 1986, *IrAJ*, 17, 294
 Carmona, A., van den Ancker, M. E., & Henning, Th. 2007, *A&A*, 464, 687
 Catala, C., Alecian, E., Donati, J.-F., et al. 2007, *A&A*, 462, 293
 Chen, C. H., Sargent, B. A., Bohac, C., et al. 2006, *ApJ Supp.*, 166, 351
 Cohen, M. 1998, *AJ*, 115, 2092
 Coulson, I. M., Walther, D. M., & Dent, W. R. F. 1998, *MNRAS*, 296, 934
 D'Angelo, G., Errico, L., Gomez, M. T., et al. 2000, *A&A*, 356, 888
 Dent, W. R. F., Greaves, J. S., & Coulson, I. M. 2005, *MNRAS*, 359, 663
 Dommanget, J., & Nys, O. 2002, *yCat*, 1/274
 Dorschner, J., Begemann, B., Henning, Th., Jaeger, C., & Mutschke, H. 1995, *A&A*, 300, 503
 Doucet, C., Habart, E., Pantin, E., et al. 2007, *A&A*, 470, 625
 Dullemond, C. P., & Dominik, C. 2004, *A&A*, 417, 159
 Dunkin, S. K., Barlow, M. J., Ryan, S. G. 1997, *MNRAS*, 290, 165
 Folsom, C. P. 2007, *Magnetic, chemical and rotational properties of the Herbig Ae/Be binary HD 72106*, Thesis at Queen's University; Kingston, Ontario, Canada
 Furlan, E., Hartmann, L., Calvet, N., et al. 2006, *ApJ Supp.*, 165, 568
 Geers, V. C., Augereau, J.-C., Pontoppidan, K. M., et al. 2005, in *High Resolution Infrared Spectroscopy in Astronomy*, ed. H. U., Käuffl, R., Siebenmorgen, & A. Moorwood (Springer), 239
 Geers, V. C., Augereau, J.-C., Pontoppidan, K. M., et al. 2006, *A&A*, 459, 545
 Geers, V. C., Pontoppidan, K. M., van Dishoeck, E. F., et al. 2007a, *A&A*, 469, L35
 Geers, V. C., van Dishoeck, E. F., Visser, R., et al. 2007b, *A&A*, 476, 279
 Green, J. D., Hartmann, L., Calvet, N., et al. 2006, *ApJ*, 648, 1099
 Habart, E., Testi, L., Natta, A., & Carillet, M. 2004, *ApJ*, 614, L129
 Habart, E., Natta, A., Testi, L., & Carillet, M. 2006, *A&A*, 449, 1067
 Hales, A. S., Gledhill, T. M., Barlow, M. J., & Lowe, K. T. E. 2006, *MNRAS*, 365, 1348
 Hallenbeck, S., & Nuth, J. 1997, *Ap&SS*, 255, 427
 Hanner, M. S., Brooke, T. Y., & Tokunaga, A. T. 1998, *ApJ*, 502, 871
 Hartmann, L., & Kenyon, S. J. 1996, *ARA&A*, 34, 207
 Henning, Th., Launhardt, R., Steinacker, J., & Thamm, E. 1994, *A&A*, 291, 546
 Herbig, G. H. 2005, *AJ*, 130, 815
 Hernández, J., Calvet, N., Briceño, C., Hartmann, L., & Berlind, P. 2004, *AJ*, 127, 1682
 Higdon, S. J. U., Devost, D., Higdon, J. L., et al. 2004, *PASP*, 116, 975
 Hillenbrand, L. A., Strom, S. E., Vrba, F. J., & Keene, J. 1992, *ApJ*, 397, 613
 Honda, M., Katata, H., Okamoto, Y. K., et al. 2006, *ApJ*, 646, 1024
 Hony, S., Van Kerckhoven, C., Peeters, E., et al. 2001, *A&A*, 370, 1030
 Houck, J. R., Roellig, T. L., van Cleve, J., et al. 2004, *ApJS*, 154, 18
 Hudgins, D. M., & Allamandola, L. J. 1999, *ApJ*, 516, L41
 Hutchinson, M. G., Evans, A., Winkler, H., & Spencer Jones, J. 1990, *A&A*, 234, 230
 Jaeger, C., Molster, F. J., Dorschner, J., et al. 1998, *A&A*, 339, 904
 Jayawardhana, R., Fisher, R. S., Telesco, C. M., et al. 2001, *AJ*, 122, 2047
 Jensen, E. L. N., & Mathieu, R. D. 1997, *AJ*, 114, 301
 Juhász, A., Henning, Th., Bouwman, J., et al. 2009, *ApJ*, in press [arXiv:0902.0405]
 Käuffl, H.-U., Sterzik, M. F., Siebenmorgen, R., et al. 2003, *SPiE*, 4841, 117
 Kemper, F., Vriend, W. J., & Tielens, A. G. G. M. 2004, *ApJ*, 609, 826
 Kenyon, S. J., Hartmann, L., & Hewett, R. 1988, *ApJ*, 325, 231
 Kenyon, S. J., Kolotilov, E. A., Ibragimov, M. A., & Mattei, J. A. 2000, *ApJ*, 531, 1028
 Kessler-Silacci, J. E., Augereau, J.-C., Dullemond, C. P., et al. 2006, *ApJ*, 639, 275
 Kessler-Silacci, J. E., Dullemond, C. P., Augereau, J.-C., et al. 2007, *ApJ*, 659, 680
 Kurucz, R. L. 1994, *Solar abundance model atmospheres for 0, 1, 2, 4, 8 km/s*, CD-ROM No. 19. (Cambridge, Mass.: Smithsonian Astrophysical Observatory)
 Lagage, P. O., Pel, J. W., Authier, M., et al. 2004, *Msngr*, 117, 12
 Lagage, P. O., Doucet, C., Pantin, E., et al. 2006, *Science*, 314, 621
 Leinert, C., Richichi, A., & Haas, M. 1997, *A&A*, 318, 472
 Leinert, Ch., van Boekel, R., Waters, L. B. F. M., et al. 2004, *A&A*, 423, 537
 Li, A., & Draine, B. T. 2002, *ApJ*, 572, 232
 Lisse, C. M., Beichman, C. A., Bryden, G., & Wyatt, M. C. 2007, *ApJ*, 658, 584
 Lisse, C. M., Chen, C. H., Wyatt, M. C., & Morlok, A. 2008, *ApJ*, 673, 1106
 Lovis, C., Mayor, M., Pepe, F., et al. 2006, *Nature*, 441, 305
 Lowrance, P. J., Schneider, G., Kirkpatrick, J. D., et al. 2000, *ApJ*, 541, 390
 Malfait, K., Bogaert, E., & Waelkens, C. 1998, *A&A*, 331, 211
 Mamajek, E. E., Meyer, M. R., Hinz, P. M., et al. 2004, *ApJ*, 612, 496
 Mannings, V., & Barlow, M. J. 1998, *ApJ*, 497, 330
 Mattioli, A. L., Hudgins, D. M., & Allamandola, L. J. 2005, *ApJ*, 629, 1188
 Meeus, G., Waters, L. B. F. M., Bouwman, J., et al. 2001, *A&A*, 365, 476
 Meeus, G., Bouwman, J., Dominik, C., Waters, L. B. F. M., & de Koter, A. 2002, *A&A*, 392, 1039
 Meeus, G., Sterzik, M., Bouwman, J., & Natta, A. 2003, *A&A*, 409, L25
 Meyer, M. R., Backman, D. E., Weinberger, A. J., & Wyatt, M. C. 2007, in *Protostars and Planets V*, ed. B. Reipurth, D. Jewitt, & K. Keil (University of Arizona Press Tucson), 573
 Moorwood, A., Cuby, J. G., & Lidman, C. 1998, *Msngr*, 91, 9
 Natta, A., Testi, L., Neri, R., Shepherd, D. S., Wilner, D. J. 2004, *A&A*, 416, 179
 Okamoto, Y. K., Katata, H., Honda, M., et al. 2004, *Nature*, 431, 660
 Oudmaijer, R. D., van der Veen, W. E. C. J., Waters, L. B. F. M., et al. 1992, *A&A Supp.*, 96, 625
 Pascucci, I., Apai, D., Hardegree-Ullman, E. E., et al. 2008, *ApJ*, 673, 477
 Pasquini, L., Cutispoto, G., Gratton, R., & Mayor, M. 1991, *A&A*, 248, 72
 Peeters, E., Hony, S., Van Kerckhoven, C., et al. 2002, *A&A*, 390, 1089
 Peeters, E., Allamandola, L. J., Hudgins, D. M., Hony, S., & Tielens, A. G. G. M. 2004a, in *Astrophysics of Dust*, ed. A. N. Witt, G. C. Clayton, & B. T. Draine, ASP Conf. Ser., 309, 141
 Peeters, E., Mattioli, A. L., Hudgins, D. M., & Allamandola, L. J. 2004b, *ApJ*, 617, L65
 Perrin, M. D., Duchene, G., Kalas, P., & Graham, J. R. 2006, *ApJ*, 645, 1272
 Pogodin, M. A., Franco, G. A. P., & Lopes, D. F. 2005, *A&A*, 438, 239
 Prato, L., Ghez, A. M., Piña, R. K., et al. 2001, *ApJ*, 549, 590
 Przygodda, F., van Boekel, R., Abraham, P., et al. 2003, *A&A*, 412, L43
 Quanz, S. P., Henning, Th., Bouwman, J., Ratzka, Th., & Leinert, Ch. 2006, *ApJ*, 648, 472
 Quanz, S. P., Henning, Th., Bouwman, J., et al. 2007, *ApJ*, 668, 359

- Quast, G. R., Torres, C. A. O., de La Reza, R., da Silva, L., & Mayor, M. 2000, *IAUS*, 200, 28
- Rietmeijer, F. J. M. 1989, in *Lunar and Planetary Science Conference, 19th, Proceedings A89-36486 15-91* (Cambridge University Press / Lunar and Planetary Institute), p. 513
- Savage, B. D., & Mathis, J. S. 1979, *ARA&A*, 17, 73
- Scheegerer, A., Wolf, S., Voshchinnikov, N. V., Przygodda, F., & Kessler-Silacci, J. E. 2006, *A&A*, 456, 535
- Schütz, O., & Sterzik, M. F. 2005, in *High Resolution Infrared Spectroscopy in Astronomy*, ed. H. U. Käufel, R. Siebenmorgen, & A. Moorwood, (Springer), 104
- Schütz, O., Meeus, G., & Sterzik, M. F. 2005a, *A&A*, 431, 165
- Schütz, O., Meeus, G., & Sterzik, M. F. 2005b, *A&A*, 431, 175
- Servoin, J. L., & Piriou, B. 1973, *Phys. Stat. Sol. B*, 55, 677
- Sheret, I., Dent, W. R. F., & Wyatt, M. C. 2004, *MNRAS*, 348, 1282
- Sicilia-Aguilar, A., Hartmann, L. W., Watson, D., et al. 2007, *ApJ*, 659, 1637
- Sloan, G. C., Hayward, T. L., Allamandola, L. J., et al. 1999, *ApJ*, 513, L65
- Sloan, G. C., Keller, L. D., Forrest, W. J., et al. 2005, *ApJ*, 632, 956
- Sloan, G. C., Jura, M., Duley, W. W., et al. 2007, *ApJ*, 664, 1144
- Smith, T. L., Clayton, G. C., & Valencic, L. 2004, *AJ*, 128, 357
- Song, I., Caillault, J.-P., Barrado y Navascués, D., & Stauffer, J. R. 2001, *ApJ*, 546, 352
- Song, I., Zuckerman, B., Weinberger, A. J., & Becklin, E. E. 2005, *Nature*, 436, 363
- Spitzer, W. G., & Kleinman, D. A. 1961, *Phys. Rev.*, 121, 1324
- Stencel, R. E., & Backman, D. E. 1991, *ApJS*, 75, 905
- Sterzik, M. F., Melo, C. H. F., Tokovinin, A. A., & van der Bliik, N. 2005, *A&A*, 434, 671
- Strassmeier, K. G., & Rice, J. B. 2000, *A&A*, 360, 1019
- Sylvester, R. J., Skinner, C. J., Barlow, M. J., & Mannings, V. 1996, *MNRAS*, 279, 915
- Sylvester, R. J., & Mannings, V. 2000, *MNRAS*, 313, 73
- Sylvester, R. J., Dunkin, S. K., & Barlow, M. J. 2001, *MNRAS*, 327, 133
- Tielens, A. G. G. M. 2008, *ARA&A*, 46, 289
- Torres, C. A. O., Quast, G., de la Reza, R., Gregorio-Hetem, J. & Lépine, J. R. D. 1995, *AJ*, 109, 2146
- Torres, G. 2004, *AJ*, 127, 1187
- Torres, C. A. O., Quast, G. R., da Silva, L., et al. 2006, *A&A*, 460, 695
- van Boekel, R., Waters, L. B. F. M., Dominik, C., et al. 2003, *A&A*, 400, L21
- van Boekel, R., Min, M., Leinert, Ch., et al. 2004, *Nature*, 432, 479
- van Boekel, R., Min, M., Waters, L. B. F. M., et al. 2005, *A&A*, 437, 189
- van den Ancker, M. E., de Winter, D., & Tjin A Djie, H. R. E. 1998, *A&A*, 330, 145
- van Dienenhoven, B., Peeters, E., Van Kerckhoven, C., et al. 2004, *ApJ*, 611, 928
- Van Kerckhoven, C. 2002, Ph.D. thesis at Catholic University of Leuven, Belgium
- Van Kerckhoven, C., Hony, S., Peeters, E., et al. 2000, *A&A*, 357, 1013
- Vieira, S. L. A., Corradi, W. J. B., Alencar, S. H. P., et al. 2003, *AJ*, 126, 2971
- Wang, H., Apai, D., Henning, T., & Pascucci, I. 2004, *ApJ*, 601, L83
- Werner, M. W., Roellig, T. L., Low, F. J., et al. 2004, *ApJS*, 154, 1
- Worley C. E., & Douglass G. G. 1997, *A&AS*, 125, 523
- Wyatt, M. C., Greaves, J. S., Dent, W. R. F., & Coulson, I. M. 2005, *ApJ*, 620, 492
- Yudin, R. V. 2000, *A&AS*, 144, 285
- Zuckerman, B., & Song, I. 2004, *ARA&A*, 42, 685
- Zuckerman, B., Song, I., Bessell, M. S., & Webb, R. A. 2001, *ApJ*, 562, L87